DAXX safeguards heterochromatin formation in embryonic stem cells

Authors: Antoine Canat (1,2), Adeline Veillet (1), Renaud Batrin (1), Clara Dubourg (1,4), Robert Illingworth (3), Emmanuelle Fabre (1), Pierre Therizols (1,4)*

Affiliation:

(1) Université de Paris, Laboratoire Génomes, Biologie Cellulaire et Thérapeutiques, CNRS UMR7212, INSERM U944, Institut de Recherche St Louis, F- 75010 Paris, France

(2) Present address: Institute of Epigenetics and Stem Cells, Helmholtz Zentrum München, München, Germany

(3) Centre for Regenerative Medicine, Institute for Regeneration and Repair, The University of Edinburgh, Edinburgh BioQuarter, 5 Little France Drive, Edinburgh EH16 4UU, United Kingdom.

(4) Present address: Université de Paris, Epigenetics and Cell Fate, CNRS, 75013 Paris, France

* Correspondence: pierre.therizols@cnrs.fr. Tel: +33-1-5727-8926

Abstract

Genomes comprise a large fraction of repetitive sequences folded into constitutive heterochromatin to protect genome integrity and cell identity. *De novo* formation of heterochromatin during preimplantation development is an essential step for preserving the ground-state of pluripotency and the self-renewal capacity of embryonic stem cells (ESCs). Yet, the molecular mechanisms responsible for the remodeling of constitutive heterochromatin are largely unknown. Here, we find that DAXX, an H3.3 chaperone, is essential for ESCs maintenance in the ground-state of pluripotency. DAXX accumulates at pericentromeric regions, and recruits PML and SETDB1, thereby promoting heterochromatin formation. In absence of DAXX or PML, the 3D-architecture and physical properties of pericentric and peripheral heterochromatin are disrupted, resulting in derepression of major satellite DNA, transposable elements and genes associated with the nuclear lamina. Using epigenome editing tools, we observe that H3.3, and specifically H3.3K9 modification, directly contribute to maintaining pericentromeric chromatin conformation. Altogether, our data reveal that DAXX is crucial for the maintenance and 3D-organization of the heterochromatin compartment and protects ESCs viability.

Keywords: Heterochromatin; Pericentromere; Chromocenters; Nuclear periphery; histone variant H3.3; DAXX; SETDB1; PML; Embryonic Stem Cell

Introduction

Eukaryotic nuclei generally contain two major genomic compartments, referred to as A and B, which respectively contain the active and inactive fractions of the genome. At the chromosome level, these compartments are characterized by alternating gene-rich and gene-poor domains. The B compartment is composed primarily of repetitive sequences, with satellite tandem repeats comprising one of the most abundant classes. Pericentromeric regions in mouse are composed of tandem repeats of a 234 bp sequence, named Major Satellite, that constitute approximately 8 Mb on each chromosome (Consortium et al., 2002; Guenatri et al., 2004). Most genes and repeated sequences of the B compartment are transcriptionally repressed by cooperative epigenetic mechanisms leading to the formation of constitutive heterochromatin. The three-dimensional organization of constitutive heterochromatin is an important layer regulating transcription (Falk et al., 2019; Lu et al., 2021). In some species, including the mouse, the pericentromeric heterochromatin (PCH) of different chromosomes aggregates to form large DAPI-dense heterochromatin clusters, called chromocenters. Disruption of satellite clustering is often associated with increased DNA damage and defects in chromosome segregation that are seen in pathologies such as Alzheimer's disease and breast cancer (Hahn et al., 2013; Jagannathan et al., 2018; Mansuroglu et al., 2016; Zhu et al., 2011). Gene-poor domains are preferentially found beneath the nuclear edge and often referred as Lamina-Associated Domains (LADs) (Guelen et al., 2008). The tethering to the nuclear envelope is stochastic, and LADs are also found associated with other nuclear landmarks such as chromocenters and nucleolus (Koningsbruggen et al., 2010; Wijchers et al., 2015).

At the molecular level, constitutive heterochromatin exhibits covalent modifications including DNA methylation, H3K9 and H4K20 trimethylation (H3K9me3 and H4K20me3). Maintenance of H3K9me3 at pericentromeric satellites relies on the SUV39H1/2 methyltransferases, whereas a distinct H3K9me3 methyltransferase, SETDB1, operates at dispersed DNA repeats and telomeres (Fukuda et al., 2018; Gauchier et al., 2019; Martens et al., 2005; Matsui et al., 2010).

Heterochromatin maintenance is intrinsically linked to chromatin replication during S phase, but also requires the incorporation of histone variants, such as macroH2A and H3.3, into chromatin independently of DNA synthesis (Buschbeck and Hake, 2017; Mendiratta et al., 2019). The histone variant H3.3 differs from the canonical histone H3 by 4 or 5 residues and is deposited throughout the cell cycle in active and inactive chromatin by different histone chaperones. These histone-binding proteins prevent promiscuous incorporation into chromatin (Szenker et al., 2011). Together with ATRX, DAXX forms a histone chaperone complex responsible for H3.3 incorporation into heterochromatin regions, including PCH, retrotransposons and telomeres (Drané et al., 2010; Elsässer et al., 2015; He et al., 2015; Lewis et al., 2010; Sadic et al., 2015). At telomeres and retrotransposons, DAXX promotes heterochromatin formation by recruiting SUV39H1/2 or SETDB1, hereby facilitating the deposition of H3K9me3 (Elsässer et al., 2015; Gauchier et al., 2019; He et al., 2015; Hoelper et al., 2017). In addition to its role in H3.3 deposition, DAXX also prevents promiscuous incorporation of H3.3 by recruiting soluble H3.3-H4 dimers to PML nuclear bodies, membrane-less hubs for post-translational modification of proteins (Delbarre et al., 2013; Delbarre et al., 2017; Lallemand-Breitenbach and Thé, 2018).

Heterochromatin is *de novo* established during early embryogenesis, involving an important remodeling of its molecular composition and 3D-organization (Burton and Torres-Padilla, 2014). However, the underlying mechanisms and their functional relevance for early development remain elusive. During preimplantation development, the DNA methylation inherited from parental gametes is erased and reaches its minimal level in the blastocyst, defining the ground-state of pluripotency (Leitch et al., 2013; Ying et al., 2008). This wave of DNA demethylation directly leads to the transcriptional upregulation of several repetitive sequences, a process that is essential for the remodeling of constitutive heterochromatin (Jachowicz et al., 2017; Lu et al., 2021; Probst et al., 2010). For instance, the upregulation of major satellite transcripts is required for PCH reorganization into chromocenters and normal developmental progression (Casanova et al., 2013; Probst et al., 2010). Yet, derepression of

91 DNA repeats correlates with high DNA damage signaling and their prolonged expression
92 results in developmental arrest, suggesting that silencing through a DNA methylation-
93 independent mechanism is required for normal embryogenesis (Jachowicz et al., 2017;
94 Ziegler-Birling et al., 2009). Polycomb group proteins were previously shown to bind and
95 facilitate silencing of repetitive sequences upon DNA hypomethylation (Saksouk et al., 2014;
96 Tosolini et al., 2018; Walter et al., 2016). However, knockout of most polycomb-related genes
97 does not impact pre-implantation embryogenesis (Aloia et al., 2013), implying that other factors
98 maintain heterochromatin in the absence of DNA methylation.

99 In mouse, both DAXX and H3.3 deletions cause genomic instability resulting in early embryonic
100 lethality with most knockout embryos failing to reach the blastocyst stage (Jang et al., 2015;
101 Liu et al., 2020; Michaelson et al., 1999). DAXX binds major satellite regions during the earliest
102 stages of development, just before PCH reorganizes to form chromocenters (Arakawa et al.,
103 2015; Liu et al., 2020). While the importance of DAXX for chromocenter formation remains
104 unknown, the viability of *Daxx*$^{-/-}$ embryos drops after chromocenter formation (Liu et al., 2020;
105 Probst et al., 2010), suggesting a direct link between DAXX function at chromocenters and
106 developmental progression. Surprisingly, *Daxx* is not required for *in vitro* culture of blastocyst-
107 derived Embryonic Stem Cells (ESCs) (Elsässer et al., 2015; He et al., 2015; Hoelper et al.,
108 2017). In ESCs, DAXX is not recruited to PCH, but rather to retrotransposons and telomeres
109 (Elsässer et al., 2015; Gauchier et al., 2019; He et al., 2015; Saksouk et al., 2014). However,
110 the recruitment of DAXX to chromatin is tightly associated with the low level of DNA methylation
111 that characterize preimplantation embryogenesis (Arakawa et al., 2015; He et al., 2015; Liu et
112 al., 2020). ESCs are typically cultured in serum-based media and accumulate high levels of
113 DNA methylation (Leitch et al., 2013), which could explain the discrepancies with *in vivo*
114 observations. ESCs can maintain low levels of DNA methylation and reach the ground-state
115 of pluripotency when grown in a serum-free medium, named 2i, but the role of DAXX for their
116 survival and the formation of PCH has yet to be addressed.

117 Here, we decipher the role played by DAXX at PCH in pluripotent ESCs. We find that DAXX is
118 essential for ground-state ESC survival. We provide evidence that DAXX localizes to
119 pericentric heterochromatin and recruits PML and SETDB1, facilitating heterochromatin
120 formation and organization through H3.3K9 modification. The deletion of *Daxx* or *Pml* impacts
121 pericentromeric heterochromatin formation altering its biophysical and clustering properties.
122 Thus, our results identify DAXX as an essential regulator preserving heterochromatin integrity
123 and maintaining the viability of ground-state ESCs.

124 **Results**

125 **DAXX is essential for ESC survival upon ground-state conversion.**

126 To assess the role of DAXX in pluripotent cells, we generated a *Daxx* knock-out (KO) ESC
127 line. We targeted exon 3 of *Daxx* using CRISPR/cas9 technology. While we confirmed the
128 absence of DAXX mRNA and protein (Fig. 1A; Fig. S1A), there were no obvious changes in
129 H3.3 protein levels in the resulting *Daxx* KO ESC line (Fig. 1A). Consistent with previous
130 reports, loss of DAXX did not impact the growth of ESCs cultured with a serum-based medium
131 (Elsässer et al., 2015). Likewise, neural differentiation induced by leukemia inhibitory factor
132 withdrawal and retinoic acid addition did not impact on cell viability in *Daxx* KO ESC (Diff., Fig.
133 1B). When the *Daxx* KO and WT ESCs were converted to the ground state, using a medium
134 with two small kinase inhibitors and vitamin C (hereafter denoted 2iV), no growth defect was
135 detected for *Daxx* KO cells after 4 days of conversion, but prolonged culture in 2iV medium
136 induced a drastic decrease in cell viability (Fig. 1B). Compared to the parental WT ESCs, only
137 12.6% of *Daxx* KO ESCs remained after 8 days of culture in 2iV (Fig. 1B). No surviving cells
138 could be detected after 9 to 10 days of conversion. We confirmed that under serum conditions,
139 ESCs have higher levels of DNA methylation than the blastocyst cells from which they are
140 derived (Fig. S1B) (Borgel et al., 2010). In contrast, ESCs cultured in 2iV, exhibit very low
141 levels of DNA methylation (Blaschke et al., 2013). Altogether, these results indicate an
142 essential role for DAXX in the maintenance of pluripotent cell survival upon ground-state
143 conversion.

144 To further investigate the impact of *Daxx* knockout, we monitored the transcriptional
145 landscapes under different conditions using RNA sequencing (RNA-seq). *Daxx* KO and WT
146 cells show only negligible differential expression of protein coding genes upon differentiation
147 with retinoic acid (Fig. S1C; Fig. S1D). We concluded that the absence of DAXX only has a
148 minor impact on transcriptome changes upon neural differentiation. This result is consistent
149 with the absence of morphological or cell growth defects observed upon differentiation and
150 confirms that DAXX is dispensable for neuronal differentiation. After 4 days of 2iV conversion
151 a substantial differential expression of genes in *Daxx* KO and WT ESCs was observed (Fig.
152 S1C). However, the global transcriptional response of *Daxx* KO ESCs to 2iV medium was
153 similar to WT ESCs (Fig. S1D). We compared the expression of 166 markers previously
154 identified as differentially expressed upon 2iV conversion (Blaschke et al., 2013). For both cell
155 lines most of these markers changed expression upon conversion according to the expected
156 pattern (Fig. S1E) supporting the conclusion that *Daxx* KO ESCs can reach the ground-state
157 of pluripotency after 4 days of 2iV conversion.

158 Overall, our data show that *Daxx* is essential for the survival of ground-state ESCs but their
159 loss of viability is unlikely caused by a conversion defect. Despite the mis-regulation of over
160 2500 genes after 4 days of 2iV conversion, no significant gene network that could explain the
161 subsequent loss of viability in *Daxx* KO ESCs could be identified.

162

163 **DAXX contributes to the transcriptional repression of DNA repeats and peripheral**
164 **heterochromatin.**

165 As DAXX is known to be responsible for H3.3 deposition in heterochromatic regions, we
166 investigated the impact of *Daxx* deletion on the transcriptional repression of the silenced
167 portion of the genome (Elsässer et al., 2015).

168 LADs make up a significant portion of the silenced compartment. To investigate the effect of
169 *Daxx* deletion on the expression of genes located in the 1180 LADs described in ESCs (Peric-

170 Hupkes et al., 2010), we compared their differential expression to that of genes not interacting
171 with the lamina (CEN). In serum and differentiated conditions, we found that LAD genes had
172 very similar differential expression to genes not located in LADs (Fig. 1C; Fig. 1D). However,
173 we observed an increase in the mRNA levels of several LAD genes normally silenced such as
174 *Casp1*, *Casp4*, and *Casp12* on chromosome 9 and *Naip6* and *Naip5* on chromosome 13, in
175 *Daxx* KO ESCs under 2iV condition (Fig. 1C; Fig. 1D; Fig. S2A). Genome-wide, the differential
176 expression of genes located in LADs was significantly increased in the 2iV condition,
177 suggesting that the presence of DAXX is necessary for proper silencing of these genes in
178 ground-state ESCs.

179 Histone modification H3K9me2 is a hallmark of LADs and generally accumulates beneath the
180 nuclear envelope (Kind et al., 2013; Peric-Hupkes et al., 2010). To assess whether the global
181 upregulation of LAD genes observed in *Daxx* KO ESCs upon 2iV conversion was associated
182 with a defect in peripheral heterochromatin assembly, we examined the accumulation of
183 H3K9me2 by immunofluorescence. In WT and *Daxx* KO ESCs grown in serum condition, the
184 H3K9me2 signal was irregularly diffuse in the nucleoplasm with a significant accumulation at
185 the nuclear edge (Fig. 1E). Quantification of H3K9me2 distribution by linescan density did not
186 show any significant difference in the enrichment of signal at the nuclear periphery between
187 WT and *Daxx* KO ESCs in serum (Fig. 1F; Fig. S2B). However, after 4 days of 2iV conversion,
188 the H3K9me2 signal remained enriched at the nuclear rim in WT converted cells, but only small
189 patches along the nuclear periphery were observed in the absence of DAXX (Fig. 1E).
190 Linescan quantification confirmed a significant decrease in H3K9me2 enrichment at the
191 nuclear periphery in *Daxx* KO ESCs (Fig. 1F). In contrast, LaminB1 accumulated normally at
192 the nuclear edge in both cell lines regardless of growing conditions, indicating no global nuclear
193 lamina assembly defects in *Daxx* KO ESCs (Fig. S2C; Fig. S2D). We therefore conclude that
194 DAXX is necessary for the maintenance of peripheral heterochromatin.

195 Overall, our observations show that *Daxx* deletion impacts the regulation of the nuclear
196 periphery by altering the tethering of peripheral heterochromatin and the transcriptional
197 silencing of genes located in LADs.

198

199 **DAXX relocates to chromocenters upon ground-state conversion.**

200 We additionally found that many endogenous retrovirus families were upregulated in *Daxx* KO
201 ESCs in serum and 2iV (Fig. 2A; Fig. S3), consistent with previous observations (Elsässer et
202 al., 2015; He et al., 2015). Several LINE1 elements, notably the L1MdT and L1MdA families,
203 not previously reported as DAXX targets, were also upregulated in pluripotent *Daxx* KO ESCs
204 (Fig. 2A; Fig. S3). The role of DAXX on transcriptional silencing was not limited to interspersed
205 repeats as we detected a strong upregulation of major satellites RNA in both serum and 2iV
206 condition in the *Daxx* KO cells (Fig. 2A; Fig.S3).

207 To investigate whether DAXX binds to major satellites in ESCs, we used immunofluorescence
208 with H3K9me3 staining to track PCH after confirming the strong correlation between H3K9me3
209 and major satellites using immuno-FISH (Fig. S4A; Fig. S4B). In both serum and 2iV
210 conditions, DAXX signal concentrated in the nucleoplasm as round foci (Fig. 2B; Fig. S4C).
211 The distribution of foci sizes was similar in both growing conditions, but a small fraction of
212 larger foci could be observed under 2iV condition. We therefore set a threshold defining small
213 and larger DAXX foci (Fig. S4D). The large DAXX foci exhibited higher levels of DAPI and
214 H3K9me3 specifically under 2iV condition, supporting that DAXX can relocate to PCH in
215 ground-state ESCs (Fig. S4E; Fig. S4F). To confirm this observation, we segmented nuclei
216 and PCH foci using DAPI and H3K9me3 signals, respectively, allowing us to measure the
217 enrichment of DAXX signal at PCH per nuclei (Fig. S4G). The level of DAXX observed at PCH
218 upon 2iV conversion was significantly higher than in the serum condition (Fig. 2C). Notably,
219 the increase in DAXX enrichment in 2iV was not homogenous among the H3K9me3 foci
220 population, but rather the result of a subset of clusters showing strong DAXX enrichment,

221 allowing us to determine a threshold to define DAXX-positive PCH (Fig. 2D). While only 14%
222 of cells showed one DAXX-positive PCH cluster in the serum condition, 83% of 2iV-converted
223 cells had at least one DAXX-positive H3K9me3 focus (Fig. 2E). A small proportion of cells
224 showed 2 or 3 or more DAXX-enriched PCH foci (16% and 5%, respectively). Interestingly, our
225 analysis revealed that DAXX-enriched PCH foci were bigger in size and had higher H3K9me3
226 staining intensities, suggesting a potential link between DAXX and H3K9me3 regulation (Fig.
227 2F; Fig. 2G).

228 Altogether, our data show that DAXX accumulates in a subset of PCH clusters in ground-state
229 ESCs, suggesting that it may play a role in the maintenance of PCH and the transcriptional
230 silencing of major satellite sequences.

231

232 **DAXX maintains pericentric heterochromatin organization in pluripotent cells.**

233 To investigate the role that DAXX might play at PCH in ground-state ESCs, we next
234 investigated whether DAXX facilitates PCH formation in ESCs. Since the loss of
235 pericentromeric silencing is generally caused by defective heterochromatin assembly and
236 often correlates with impaired clustering of chromocenters (Hahn et al., 2013; Healton et al.,
237 2020; Pinheiro et al., 2012; Zhu et al., 2011), we performed DNA FISH experiments against
238 the major satellites and segmented the 3D signal to determine the number of clusters (Fig.
239 3A). In serum or differentiated cells, the deletion of *Daxx* had no significant impact on the
240 number of clusters (Fig. 3B). However, after 4 days of 2iV conversion, the average number of
241 major satellite foci was increased by 37% in the *Daxx* KO ESCs. The presence of an increased
242 number of PCH foci indicates that DAXX is required for their clustering in ESCs, specifically
243 under 2iV condition and correlates with the loss of viability observed in these cells at later
244 stages of conversion (Fig. 1B). To confirm the role of DAXX in PCH clustering, we used the
245 TALE (transcription activator–like effector) epigenome editing tool to ask whether direct DAXX
246 recruitment to major satellites was sufficient to reduce the number of foci. We generated a

247 FLAG-tagged TALE engineered to specifically target major satellite sequences (hereafter
248 called $TALE_{MajSat}$), following the design of a previous study (Miyanari et al., 2013).
249 Immunofluorescence against the FLAG tag of the $TALE_{MajSat}$ confirmed its colocalization with
250 the major satellite FISH signal (Fig. 3C). When bound to pericentromeres in pluripotent *Daxx*
251 KO cells, $TALE_{MajSat}$-DAXX restored chromocenter clustering with the formation of fewer PCH
252 foci (Fig. 3D). In WT ESCs, artificial tethering of DAXX to chromocenters had a similar impact,
253 increasing endogenous PCH clustering (Fig. S5A). These results indicate that DAXX enhances
254 physical interactions between major satellite sequences and contributes to the 3D organization
255 of PCH.

256 We hypothesized that the decreased chromocenter clustering seen in *Daxx* KO ESCs might
257 result from defective heterochromatin formation. Functional heterochromatin forms a self-
258 segregating subcompartment with limited protein exchange with the rest of the nucleoplasm
259 (Hinde et al., 2015; Strom et al., 2017). To test whether DAXX is important for heterochromatin
260 segregation, we followed GFP-HP1α using live-imaging in WT and *Daxx* KO ESCs (Fig. 3E).
261 We monitored the mobility of GFP-HP1α by measuring its fluorescence recovery rate at
262 chromocenters after photobleaching (Fig. 3E; Fig. S5B). Compared to WT, the half-recovery
263 time was significantly shorter in *Daxx* KO cells both in serum and 2iV conditions, suggesting
264 higher protein exchange between chromocenter and the nucleoplasm in the absence of DAXX
265 (Fig. 3F). However, the mobile fraction of GFP-HP1α remained constant in both cell lines,
266 suggesting that the same amount of protein was bound to chromatin (Fig. S5B).

267 The boundary property of PCH is known to cause high variance in HP1α signal over time at
268 the edge of a chromocenter (Strom et al., 2017). We reasoned that this higher HP1α recovery
269 rate might arise from altered heterochromatin acting as a barrier to protein diffusion. We thus
270 quantified temporal changes in GFP-HP1α signal intensity variation at unbleached
271 chromocenters (Fig. 3G). We found that variance levels were low in the nucleoplasm of WT
272 ESCs and only increased at chromocenters, peaking at their borders (Fig. 3G; Fig. 3H),
273 confirming previous observations (Strom et al., 2017). However, in *Daxx* KO cells, the pattern

274 of the variance from HP1α signal was altered. In both serum and 2iV conditions, the peak of
275 variance at the edge of chromocenters was significantly lower in the absence of DAXX,
276 suggesting a compromised heterochromatin barrier (Fig. 3H). Moreover, molecular analysis
277 using MNase digestion revealed that *Daxx* deletion in pluripotent ESCs increased the
278 accessibility of pericentric chromatin, indicating that PCH exists in an abnormal state in these
279 cells (Fig. S5C).

280 Altogether, our data suggests that DAXX plays a crucial role in regulating PCH compaction
281 state, chromocenter boundary properties, and major satellite clustering. In conclusion, DAXX
282 is essential for proper assembly and spatial organization of pericentromeric heterochromatin
283 in pluripotent ESCs.

284

285 **PML and DAXX share similar roles in ESCs.**

286 PML, identified as a partner of DAXX, has been recently shown to contribute to the
287 transcriptional repression of transposable elements in ESCs (Tessier et al., 2022). To
288 investigate the role of PML in the organization of the heterochromatic compartment in ground-
289 state ESCs, we first analyzed its localization in relation to DAXX and H3K9me3 by
290 immunofluorescence (Fig. 4A; Fig. S6A). Independently of culture conditions, PML formed
291 small round foci within the nucleoplasm that colocalized with DAXX, known as nuclear bodies
292 (Fig. 4A; Fig. S6A). Upon 2iV conversion, a fraction of larger PML foci were observed with
293 higher levels of H3K9me3 and DAPI (Fig. S6B; Fig. S6C; Fig. S6D). These larger PML foci
294 accumulated around PCH in the form of either complete or partial structures, referred to as
295 PML-rim or PML-arc, respectively (Fig. 4A; Fig. S6E). Both the PML-rim and PML-arc
296 structures were consistently associated with the presence of DAXX at PCH and were observed
297 in similar proportions as DAXX-positive PCH clusters (Fig. 2E; Fig. 4B). This indicates that
298 PML is recruited to PCH alongside DAXX in ground-state ESCs.

299 To further examine the role played by PML at PCH clusters, we analyzed the distribution of
300 major satellites in *Pml* KO ESC using FISH (Tessier et al., 2022). In *Pml* KO ESCs, no protein
301 was detectable (Fig. S7A). Similar to the *Daxx* KO line, *Pml* KO ESCs showed a significant
302 increase in the number of major satellite foci only after 4 days of 2iV conversion (Fig. 4C; Fig.
303 4D), suggesting that PML, like DAXX, is required for proper PCH clustering in ground-state
304 ESCs.

305 The integrity of peripheral heterochromatin in *Pml* KO ESCs was analyzed.
306 Immunofluorescence revealed that H3K9me2 accumulated at the nuclear periphery to a
307 greater extent in serum conditions in *Pml* KO cells compared to WT cells (Fig. 4E; Fig. 4F).
308 However, after 4 days of 2iV conversion, the H3K9me2 signal in *Pml* KO cells was similar to
309 that observed in *Daxx* KO cells, with only small patches of H3K9me2 present beneath the
310 nuclear envelope and a significant reduction in peripheral enrichment of the signal (Fig. 4F).
311 In contrast, LaminB1 signal was not altered by Pml deletion supporting the conclusion that it is
312 specific to peripheral heterochromatin (Fig. S7B; Fig. S7C). To determine the effect of this
313 alteration of peripheral heterochromatin on gene expression, we analyzed the transcriptional
314 repression of LAD genes that were upregulated after *Daxx* deletion. Out of the six selected
315 genes, five showed higher mRNA levels in 2iV-converted *Pml* KO ESCs compared to WT cells
316 (Fig. 4G). Although the transcriptional upregulation was less severe in *Pml* KO cells than in
317 *Daxx* KO cells, our results suggest that PML, like DAXX, is involved in the transcriptional
318 silencing of LAD genes.

319 The deletion of *Pml* and *Daxx* have very comparable consequences on the heterochromatin
320 of ESCs after 4 days of 2iV conversion. We thus wondered how *Pml* deletion would impact the
321 viability of ESCs under prolonged 2iV conversion (Fig. 4H). After 4 days of conversion, the
322 viability of *Pml* KO was not impacted, but was decreased by nearly 75% after 8 days. Like the
323 deletion of *Daxx*, this effect was specific to prolonged 2iV conversion as the absence of PML
324 had no consequence on the viability under serum condition or after retinoic acid differentiation.

325 Overall, our data show that PML and DAXX play similar roles in ground-state ESCs. Like
326 DAXX, PML is recruited to PCH and its absence impairs the proper organization of the
327 heterochromatic compartment, significantly impacting cell viability.

328

329 **DAXX recruits SETDB1 to chromocenters in ground-state ESCs.**

330 We have shown that in ground-state ESCs, DAXX and PML are recruited to major satellites
331 thereby facilitating PCH formation. To further investigate the mechanism underlying the
332 function of DAXX and PML, we searched for DAXX- and PML-interacting factors that could be
333 recruited specifically to chromocenters. Amongst the DAXX interacting partners, SETDB1, an
334 H3K9me3 methyltransferase, colocalizes with DAXX at PML nuclear bodies and is important
335 for repetitive DNA transcriptional silencing (Cho et al., 2011; Karimi et al., 2011). SETDB1
336 partially colocalized with PML in a DAXX-independent manner in serum conditions (Fig. S8A).
337 Under 2iV treatment, SETDB1 relocalized to PCH with DAXX and PML in 70% of WT ESCs
338 (Fig. 5A; Fig. 5B; Fig. S8B). By contrast, PML and SETDB1 were only associated with PCH in
339 5 and 17% of *Daxx* KO cells, respectively (Fig. 5B). We conclude that DAXX is critical for PML
340 and SETDB1 recruitment to chromocenters. To confirm that DAXX was sufficient for SETDB1
341 recruitment to PCH, we expressed $TALE_{MajSat}$, fused to DAXX in *Daxx* KO ESCs. TALE-
342 mediated DAXX binding to major satellite repeats drastically increased the amount of SETDB1
343 signal observed at chromocenters (Fig. S8C; Fig. S8D).

344 The presence of DAXX at PCH correlated with higher amounts of H3K9me3 in 2iV condition
345 (Fig. 2G). However, DAXX deletion had no effect on H3K9me3 levels at chromocenters
346 independently of culture conditions (Fig. S9A; Fig. S9B). Since DAXX deletion prevented
347 SETDB1 recruitment to PCH, it suggests that the majority of H3K9me3 deposition at this locus
348 relies on, or can be rescued by other lysine methyl transferases, such as SUV39H1/2 (Lehnertz
349 et al., 2003; Peters et al., 2001).

350 To further investigate the conflicting results of DAXX-mediated SETDB1 recruitment and the
351 unchanged amount of H3K9me3 in *Daxx* KO ESCs, we examined the individual roles of DAXX,
352 SETDB1, and H3K9me3 in PCH spatial organization. We used Suv39H1/2 double knock-out
353 (Suv39dKO) ESCs, in which H3K9me3 can only result from SETDB1 activity. Suv39dKO cells
354 did not show any growth defects in 2iV medium, indicating the dispensability of both enzymes
355 for pluripotency. Unlike WT ESCs, Suv39dKO did not accumulate H3K9me3 at major satellite
356 foci, (Fig. S9A; Fig. 5C). However, we observed a strong accumulation of H3K9me3 in some
357 major satellite foci surrounded by PML upon 2iV conversion, suggesting that the fraction of
358 SETDB1 recruited to PCH in ground state is indeed functionally active (Fig. 5C; Fig. 5D). We
359 next used the $TALE_{MajSat}$ strategy to specifically target DAXX, SETDB1 or SUV39H1 to
360 chromocenters in Suv39dKO ESCs (Fig. 5E). Both histone methyltransferases were able to
361 individually restore H3K9me3 at chromocenters, when targeted by $TALE_{MajSat}$ (Fig. 5E; Fig
362 S9C). The specific recruitment of DAXX to major satellite foci also promoted H3K9me3
363 deposition via SETDB1, at 70% of chromocenters. The impact of the different $TALE_{MajSat}$
364 fusions on PCH clustering was further assessed by quantifying the number of TALE-bound foci
365 (Fig. 5F). Consistent with our observations in *Daxx* KO and WT ESCs (Fig. 3D, S5A) targeting
366 DAXX to major satellite also enhanced PCH clustering in Suv39dKO ESCs as evidenced by
367 the reduced number of PCH foci (Fig. 5F). However, the recruitment of either SETDB1 or
368 SUV39H1 did not affect the number of chromocenters, supporting the conclusion that
369 H3K9me3 modification does not influence PCH clustering (Fig. 5F).

370 Overall, our results demonstrate that DAXX recruits a catalytically active SETDB1 to PCH upon
371 2iV conversion. However, SETDB1 and H3K9me3 modification alone are not sufficient to
372 mediate PCH clustering, confirming that DAXX plays a central role in PCH organization in
373 ground-state ESCs.

374

375 **H3.3K9 modification is crucial for PCH organization**

376 Since DAXX, unlike SETDB1, had a direct impact on the spatial organization of chromocenters,
377 we examined the role of H3.3 chaperone activity of DAXX by expressing a mutated form,
378 $DAXX^{Y222A}$, that lowers its interaction with H3.3 (Elsässer et al., 2012). We confirmed that co-
379 immunoprecipitation of $TALE_{MajSat}$ $DAXX^{Y222A}$ fusion with H3.3 was drastically reduced
380 compared to its wild-type counterpart (Fig. S9D). While targeting DAXX to chromocenters
381 could recruit a tagged version of H3.3, neither the control $TALE_{MajSat}$ nor $TALE_{MajSat}$ $DAXX^{Y222A}$
382 fusion were able to mobilize H3.3 to PCH (Fig. S9E; Fig. S9F). When expressed in Suv39dKO
383 ESCs, the $TALE_{MajSat}$ $DAXX^{Y222A}$ fusion did not increase H3K9me3 levels at chromocenters, as
384 it failed to recruit SETDB1 (Fig. 5E; Fig. S8C; Fig. S8D). Importantly, expressing the $DAXX^{Y222A}$
385 mutant in *Daxx* KO ESCs did not change the number of chromocenters arguing that H3.3 is
386 crucial for DAXX-mediated PCH clustering (Fig. 5F). To further confirm a function for H3.3 in
387 chromocenter organization, we depleted endogenous H3.3 using a pool of siRNAs targeting
388 the 3'UTR of H3f3a/b mRNAs and expressed $TALE_{MajSat}$-DAXX in *Daxx* KO ESCs (Fig. 5G;
389 Fig. S9E). The H3.3 knock-down was rescued by the expression of different HA-tagged
390 versions of H3.3, which were assessed for their impact on PCH clustering by immuno-FISH
391 (Fig. 5G, S9G). The binding of DAXX at major satellite did not enhance PCH clustering when
392 H3.3 was knocked down. The expression of a wild-type H3.3-HA significantly reduced the
393 number of major satellite foci and rescued the PCH hyperclustering phenotype mediated by
394 $TALE_{MajSat}$-DAXX. In contrast, expression of $H3.3^{G90M}$, a mutant unable to bind DAXX (Elsässer
395 et al., 2012; Hoelper et al., 2017), did not decrease the number of major satellite foci (Fig. 5H).
396 This result is consistent with the absence of a chromocenter clustering phenotype in cells
397 transfected by $TALE_{MajSat}$- $DAXX^{Y222A}$ (Fig. 5F) and confirms the important role of H3.3 in PCH
398 clustering. Since DAXX can recruit SETDB1 to PCH, we asked whether a H3.3K9 mutant that
399 cannot be methylated impacts PCH clustering and used $H3.3^{K9A}$. Like $H3.3^{G90M}$, $H3.3^{K9A}$ failed
400 to rescue the hyper-clustering phenotype in $TALE_{MajSat}$-DAXX expressing cells, suggesting that
401 the modification of this residue is essential for the spatial organization of chromocenters (Fig.
402 5H).

403 Altogether, we conclude that the role of DAXX in PCH organization is intrinsically linked to its
404 chaperone activity. Interaction with H3.3 and H3.3K9 modifications are important in facilitating
405 the spatial organization of pericentromeres in pluripotent ESCs.

406

407 ## Discussion

408 During early embryogenesis, adapting heterochromatin to compensate for the wave of DNA
409 demethylation is essential to maintain transcriptional repression of repetitive DNA and protect
410 genome integrity. The mechanisms and molecular factors responsible for heterochromatin
411 reorganization were, however, largely unknown. Here, we describe a novel and essential role
412 for the H3.3-chaperone DAXX and its partner PML in the survival of ground-state pluripotent
413 stem cells. Taken together, our results support a model in which DAXX and PML facilitate both
414 pericentric and peripheral heterochromatin formation in ground-state ESCs (Fig. 6). At PCH,
415 DAXX deposits H3.3 and recruits PML and SETDB1, which can methylate H3.3K9. In the
416 absence of either DAXX or PML, PCH is compromised (Fig. 6). In *Daxx* KO ESCs,
417 heterochromatin at major satellite is less compact and partially loses its boundary properties
418 leading to defective chromocenter clustering. At the nuclear periphery, PML and DAXX are
419 necessary for the maintenance of the heterochromatin positioned beneath the nuclear
420 envelope, contributing to the transcriptional silencing of genes tethered to the nuclear lamina.
421 The global failure in heterochromatin compartment formation could directly contribute to the
422 impossibility of *Daxx* KO and *Pml* KO ESCs to maintain the ground-state of pluripotency.

423 ### DAXX and H3.3 impact chromocenter organization

424 Both DAXX and H3.3 are essential for early embryogenesis, but their specific functions have
425 remained elusive (Jang et al., 2015; Lin et al., 2013; Liu et al., 2020; Michaelson et al., 1999).
426 we found that DAXX is necessary for maintaining the spatial organization and chromatin state
427 of pericentric heterochromatin (PCH), thereby protecting the viability of ground-state ESCs
428 (Fig. 3B; Fig. 3F; Fig. 3H). This finding is consistent with *in vivo* observations, which show that

429 DAXX and SETDB1 are recruited to PCH just before chromocenter formation, and the viability
430 of *Daxx* KO embryos drops quickly after the transition to the pluripotent stage (Arakawa et al.,
431 2015; Cho et al., 2012; Liu et al., 2020). These observations support our conclusion that the
432 role of DAXX and SETDB1 at PCH might be crucial for the ground-state of pluripotency. Since
433 defective PCH assembly is often associated with genomic instability, our model may also
434 explain why *H3f3a/b* double knockout ESCs exhibit severe chromosome segregation defects
435 (Jang et al., 2015).

436 While *Daxx* deletion had no impact on major satellite transcription and chromocenter formation
437 upon neuronal differentiation (Fig. 2A; Fig. 3B), DAXX and H3.3 are important for chromocenter
438 clustering during myoblast differentiation (Park et al., 2018; Salsman et al., 2017). In
439 myoblasts, DAXX is recruited to chromocenters, where H3.3 deposition stimulates
440 transcription of major satellites, suggesting a mechanism different to the one we observed in
441 ESCs. Different DAXX and partner recruitment pathways could explain the opposite impact of
442 DAXX and H3.3 on major satellite transcription. In ESCs, DAXX recruits SETDB1, thus favoring
443 a repressive chromatin environment. Upon myoblast differentiation, *Setdb1* is downregulated
444 and might not be available for interaction with DAXX, which is recruited to major satellite
445 repeats by the muscle-specific lncRNA ChRO1 (Park et al., 2018; Song et al., 2015).

446 Recent insights into chromocenter organization have come from the observation that the
447 intrinsically disordered regions of HP1α facilitate the compartmentalization of chromocenters
448 through liquid-liquid phase separation (Larson et al., 2017; Strom et al., 2017). Since the first
449 fifty amino-acids and the C-terminal half of DAXX are intrinsically disordered (Escobar-Cabrera
450 et al., 2010), it is possible that DAXX may also undergo liquid-liquid phase separation.
451 Multivalent interactions between chromodomains recognizing H3K9me3 have also been
452 proposed to contribute to phase separation of heterochromatin (Wang et al., 2019). Yet, *Daxx*
453 deletion impacted the boundary properties of pericentromeric heterochromatin without
454 affecting H3K9me3 (Fig. 3H; Fig. S9A). Since DAXX-mediated chromocenter clustering relies

455 on H3.3K9 modification (Fig. 5H), future work will compare the interaction of HP1α and
456 additional heterochromatin-related proteins to H3.3K9me3 vs. H3K9me3.

457 **Mechanism of DAXX targeting to pericentric heterochromatin**

458 In ground-state ESCs, DAXX binds only a subset of chromocenters in approximatively 80% of
459 the population (Fig. 2E). Given that chromocenters replicate synchronously during mid-S
460 phase (Guenatri et al., 2004), the recruitment of DAXX is unlikely to rely on replicative
461 chromatin remodeling. DNA hypomethylation could be one of the factors responsible for DAXX
462 mobilization to PCH. Polycomb group proteins have been shown to be recruited to PCH
463 specifically under hypomethylated conditions (Pailles et al., 2022; Saksouk et al., 2014;
464 Tosolini et al., 2018). The fact that DAXX was shown to rely on PRC1 to bind major satellites
465 in zygotes would support a polycomb-mediated recruitment of DAXX in ground-state ESCs
466 (Liu et al., 2020). However, the presence of H3K27me3, deposited by PRC2, is relatively
467 homogenous amongst the PCH foci within a nucleus, suggesting a different mechanism
468 (Tosolini et al., 2018).

469 DNA damage may also be a factor in the recruitment of DAXX to PCH. Several studies have
470 described the incorporation of H3.3 after DNA damage (Adam et al., 2013; Fortuny et al., 2021;
471 Juhász et al., 2018; Li and Tyler, 2016; Luijsterburg et al., 2016). Both HIRA and DAXX-ATRX
472 complexes have been proposed to deposit H3.3 after DNA damage, but DAXX has been more
473 specifically observed at chromocenters damaged by UVC (Fortuny et al., 2021). Active DNA
474 demethylation may be a source of DNA damage responsible for DAXX recruitment. DAXX
475 relocation to PCH was specific to the 2iV culture condition (Fig. 2B), a medium that was shown
476 to stimulate TET enzymes activity (Blaschke et al., 2013). *In vivo*, DAXX binds preferentially
477 paternal chromosomes which are actively demethylated by the TET enzymes, a pathway that
478 can result ultimately in a DSB (Nakatani et al., 2015; Wossidlo et al., 2011).

479 **Role of SETDB1 at chromocenters in ground-state ESCs**

480 SETDB1 has been shown to be responsible for H3K9me3 deposition at transposable elements
481 and telomeres (Elsässer et al., 2015; Gauchier et al., 2019; Karimi et al., 2011). Yet, knocking
482 down SETB1 in Suv39h1/h2 double knock-out cells destabilizes chromocenters suggesting
483 that SETDB1 could be involved in PCH formation (Pinheiro et al., 2012). Our data show that
484 the chaperone activity of DAXX is necessary to recruit SETDB1 to pericentromeric
485 heterochromatin (Fig. S8C). In contrast to SUV39H1/H2, SETDB1 contains a triple Tudor
486 domain recognizing the double modification K14 acetylation and K9 methylation that may
487 facilitate its binding to hyperacetylated, newly incorporated histone H3.3 (Jurkowska et al.,
488 2017). Using ESCs lacking Suv39h1/h2, we found that SETDB1 can deposit H3K9me3 at
489 chromocenters (Fig. 5C; Fig. 5D). This function of SETDB1 is consistent with its role at
490 transposable element in ESCs (Elsässer et al., 2015; Hoelper et al., 2017). Yet, it contrasts
491 with the observation that SETDB1 promotes H3K9me1 at major satellites in mouse embryonic
492 fibroblasts (Loyola et al., 2009). However, SETDB1 was specifically recruited during S-phase
493 by the H3.1/H3.2 chaperone, CAF1, suggesting that SETDB1 substrate specificity might
494 change depending on its recruitment pathway. Similar to our data in ESCs, CAF1 recruited
495 SETDB1 to chromocenters only in a subset of S-phase cells. Since pericentromeric satellites
496 were shown to be particularly sensitive to replicative stress, SETDB1 recruitment could also
497 result from DNA damage (Crosetto et al., 2013).

498 **The role of DAXX and H3.3 upon DNA hypomethylation**

499 This study reveals that DAXX is recruited to pericentromeres in the context of DNA
500 hypomethylation. While PML nuclear bodies are generally devoid of chromatin, PML formed a
501 shell around DAXX-positive chromocenters in hypomethylated ground-state ESCs (Fig. 4A).
502 Similar structures have been observed in patients with immunodeficiency, centromeric
503 instability and facial dysmorphia (ICF) syndrome associated with mutations in DNA
504 methyltransferases (Luciani et al., 2006). In patient lymphocytes, DAXX and DNA repair
505 proteins accumulate at hypomethylated pericentromeric satellites, suggesting that our
506 proposed model could apply to other pathologies (Fig. 6).

507 In conclusion, our study reveals DAXX as an important factor for different heterochromatic
508 compartments in ground-state ESCs. At the nuclear periphery, DAXX and its partner PML are
509 necessary for the clustering of peripheral heterochromatin at the nuclear edge. At PCH, DAXX
510 deposits H3.3 and recruits PML and SETDB1 to facilitate chromocenter formation by
511 enhancing their clustering properties. It would be interesting to characterize whether DAXX
512 also contributes to the 3D-organization of other heterochromatin domains, such as the
513 clustering of LINE1 elements (Lu et al., 2021). Beyond early development, our work could also
514 provide critical insights into the molecular pathways that overcome DNA hypomethylation
515 transitions in pathological contexts, such as cancers.

516

517 **Material and Methods**

518 ***Cell lines***

519 Feeder-free E14 mES cells were used for most experiment excepts otherwise notified. E14
520 mES cells were kindly provided by Pablo Navaro (Pasteur Institute). *Daxx* KO cell line was
521 constructed using CRISPR/cas9 editing in E14 mES cells. Guide-RNA was designed using the
522 online CRISPOR tool. Oligos were designed with a BbsI site on 5' to clone them into the
523 pSpCas9(BB)-2A-Puro(pX459) v2.0 vector (Ran et al., 2013). Guide was designed carrying
524 two guanines on 5' of the sequence to avoid off-target effects, as previously described (S. W.
525 Cho et al., 2014). Sg-mDaxx: gGACCTCATCCAGCCGGTTCA. *Pml* KO ESCs were generated
526 by CRISPR from E14 cells and described in a previous study (Tessier et al., 2022). Feeder-
527 free Suv39HdKO and corresponding WT R1 ES cells were provided by Alice Jouneau and
528 generated in Antoine Peters's laboratory (Lehnertz et al., 2003).

529 ***Culture conditions***

530 Pluripotent cells were cultured either in a serum condition, defined as follow: DMEM (Gibco),
531 supplemented with 10% of ESC-certified FBS (Gibco), 2-mercaptoethanol (0.05mM, Gibco),
532 Glutamax (Gibco), MEM non-essential amino acids (0.1mM, Gibco), Penn-Strep (100units/mL,

533 Gibco) and LIF (1000units/mL,) for serum condition. Serum-cultivated cells were grown on
534 0.1% gelatin-coated plates or stem cell plates (Stem Cell technology) at 37°C with 5% CO2.
535 Medium was changed every day and cells were passaged every 2 to 3 days. The other culture
536 condition is the chemically defined serum-free 2i condition defined as follow:
537 Neurobasal:DMEM/F-12 (50:50, Gibco) medium, supplemented with N2 and B-27
538 supplements (Gibco), BSA fraction V (0.05%Gibco), 1-thioglycerol ($1.5x10^{-4}$M, Sigma) and
539 ESGRO 2 inhibitors (GSK3i and MEKi) and LIF (Merck). Vitamin C (L-ascorbic acid 2-
540 phosphate, Sigma) was added at a concentration of 100µg/mL (Blaschke et al., 2013). Cells
541 were grown on 0.1% gelatin-coated plates. Medium was changed daily. Cells were passed
542 every 2 days at 1:4 ratio for the first passage then at a 1:6 ratio. Differentiation of mES cells
543 was done by LIF removal for the first 24h. Then, non-LIF medium was supplemented with
544 retinoic acid (10^{-6}M,) for 4 days. For cell growth quantification, cells were counted at each
545 passage for at least 2 different experiments.

546 ***Vectors and transfections***

547 Cells were harvested using trypsin and one million was plated in a 0.1% gelatin-coated plate
548 and transected with 0.2 to 2.5µg of DNA using the Lipofectamine 2000 reagent (Thermo),
549 following manufacturer's protocol. TALE vectors were constructed using previously described
550 methods (Ding et al., 2013). A TALE specific DNA binding domain targeting *Major Satellite*
551 repeats was created by the modular assembly of individual TALE repeats inserted into a
552 backbone vector containing TALE-Nrp1-VP64 previously described (Therizols et al., 2014).
553 The BamHI-NheI fragment containing VP64 was replaced by PCR products encoding the
554 DAXX protein, corresponding DAXX mutants or additional proteins such as SUV39H1 and
555 TET1CD. CDS of the different proteins were amplified by PCR from cDNAs obtained after RNA
556 extraction of serum E14 mES cells. DAXX mutants were generated by PCR from WT DAXX.

557 Oligos for major satellites targeting were designed with a BbsI site on 5' to clone them into the
558 pSpCas9(BB)-2A-Puro(pX459) v2.0 vector (Ran et al., 2013). Catalytically dead Cas9 (dCas9)
559 was inserted into the pSpCas9-2A-Puro(pX459) v2.0 to generate a SpdCas9-2A-Puro.

560 Target sequences for the TALE repeat domains and dCas9 associated guides RNA are listed
561 in supplementary table.

562 ***RNA extraction for RNAseq or RT-qPCR***

563 Total RNA was extracted using RNeasy extraction kit (Qiagen) according with manufacturer's
564 protocol including DNAseI treatment for 15min at room temperature (Qiagen). Complementary
565 DNA were generated from 1µg of RNA using the Maxima first strand cDNA synthesis kit
566 (Thermo Fisher), with a second round of DNAseI from the Maxima kit for 15min. Real-time
567 qPCR was carried out using a LightCycler 480 instrument (Roche) and the LightCycler 480
568 SYBR green master mix (Roche). The qRT-PCR primers used in this study are listed in
569 supplementary table. Three independent biological repeats were obtained for each sample.
570 For RNAseq experiment, RNA quality was assessed using the Agilent 2100 bioanalyzer.
571 Libraries were prepared using oligo(dT) beads for mRNA enrichment, then fragmented and
572 reverse transcribed using random hexamers primer. After adaptor ligation, the double-stranded
573 cDNA is completed through size selection of 250-300bp and PCR amplification, then quality of
574 the library is assessed by the Agilent 2100 bioanalyzer. Sequencing was performed in 150bp
575 paired-end reads using an Illumina sequencer platform.

576 ***RNA-seq Mapping and Processing***

577 FASTQ files generated by paired end sequencing were aligned to the mouse genome using
578 bowtie2 v2.2.6 (parameters: --local --threads 3; mm9 genome build). Mapped RNA-seq data
579 was processed using tools from the HOMER suite (v4.8). SAM files were converted into tag
580 directories using 'makeTagDirectory' (parameters: -format sam -sspe). Genomic intervals
581 which extended beyond the end of the chromosomes was removed using
582 'removeOutOfBoundsReads.pl'. bigWig browser track files were generated using
583 'makeUCSCfile' (parameters: -fsize 1e20 -strand + -norm 1e8). For gene expression analysis,
584 read depths were quantified for all annotated refseq genes using analyzeRepeats.pl
585 (parameters: rna mm9 -strand both -count exons -rpkm -normMatrix 1e7 -condenseGenes).

586 For repeat analysis, read coverage was quantified for each repeat and then condensed to a
587 single value for each named entry (parameters: repeats mm9 -strand both -rpkm -normMatrix
588 1e7 -condenseL1). Read depths were then corrected for the number of instances of each
589 repeat prior to expression analysis.

590 ***Expression Analysis***

591 Quantified RNA-seq data was processed using the limma package (R/Bioconductor)(Team,
592 2017). Following the addition of an offset value (1 RPKM) to each gene or repeat, data was
593 normalised across all samples using 'normalizeBetweenArrays' with method='quantile'. Fold-
594 changes and p-values for differential expression of genes and repeats were determined using
595 empirical Bayes statistics. Briefly, data was fit to a linear model using 'lmFit' and specified
596 contrasts were applied using 'makeContrasts' and 'contrasts.fit'. Data was processed using the
597 'topTable' function with adjust.method="BH" (Benjamini-Hochberg multiple-testing correction).
598 Differential expression was defined as log2 fold change ≤-1 or ≥ 1 and an adjusted p-value of
599 ≤ 0.01. Three biological replicates for each condition represent independently cultured pools
600 of cells.

601 ***Data visualization***

602 Heatmaps and boxplots were generated using Prism GraphPad (v9). Histograms were drawn
603 using either Prism GraphPad or Excel. Volcano plots were generated using the plot function in
604 R.

605 ***Immunofluorescence***

606 Murine ES cells were harvested with trypsin (Gibco) and plated for 4-12h onto either 0.1%
607 gelatin-coated or ECMatrix-coated (Sigma) glass cover slips. Cells were fixed with 4%
608 paraformaldehyde for 10min at room temperature, then rinsed three times with PBS. Cells
609 were permeabilized with 0.1X triton for 12min at room temperature, then rinsed three times
610 with PBS. Blocking was done in 3% BSA solution for 30min at room temperature. All
611 incubations with primary antibodies were performed for either 1h at room temperature or

612 overnight at 4°C with the following antibodies for H3K9me3 (Active Motif, 1:1000), DAXX
613 (Santa Cruz, 1:500), H3K9me2 (Active Motif, 1:1000), LaminB1 (Abcam, 1:1000), PML () and
614 SETDB1 (Proteintech, 1:100). Incubation with secondary antibodies (fluorescently labeled anti-
615 mouse or anti-rabbit, 1:1000) were performed for 1h at room temperature. Mounting was
616 performed using ProLong Diamond with DAPI mounting media (Thermo). Antibodies are listed
617 in supplementary table.

618 ***Fluorescent in situ Hybridization***

619 Murine ES cells were harvested with trypsin (Gibco) and plated for 4-6h onto 0.1% gelatin-
620 coated glass cover slips. Cells were fixed with 4% paraformaldehyde (PFA) for 10min at room
621 temperature, then rinsed three times with PBS. Cells were permeabilized with 0.5X triton for
622 12min at room temperature, then rinsed three times with PBS. Cells were briefly washed in 2X
623 SSC, then treated with RNAseA (100µg/mL, Sigma) for 1h at 37°C. Cells were briefly washed
624 in 2X SSC, then denatured by serial 2min incubation into 70,90 and 100% ethanol. Cover slips
625 were air dried for 15min. Cover slips are incubated with 200nM of PNA probe, placed for 10min
626 at 95°C for denaturation, then placed for 1h at room temperature in the dark for hybridization.
627 Cover slips were washed twice in 2X SSC 0.1%Tween-20 for 10min at 60°C. Cover slips were
628 immerged at room temperature in 2X SSC 0.1%Tween-20 for 2 min, then in 2X SSC for 2min
629 and 1X SSC for 2min. Mounting is performed using ProLong Diamond with DAPI mounting
630 media (Thermo).

631 ***Dot blot experiments***

632 DNA extraction was performed using the Wizard genomic DNA extraction kit (Promega).
633 Genomic DNA (1µg) was then denatured in 0.1M NaOH for 10min at 95°C before neutralization
634 with 1M NH4OAc on ice for 5min. DNA samples were spotted on a nitrocellulose membrane.
635 Blotted membrane was washed in 2X SSC and dried at 80°C for 5min before UV cross-linking
636 at 120,000µJ/cm2. Membrane was then blocked using PBS, 5% milk 0.1% tween for 30min at
637 room temperature. Membrane was incubated with 5mC antibody (Diagenode, 1:1000) for 3h

638 at room temperature. After 3 washes of 10min each in PBS, membrane was blocked again for
639 30min and then incubated with secondary anti-HRP antibody for 1h at room temperature.
640 Membrane was washed 3 times for 10min in PBS and visualized by chemiluminescence with
641 ECL Plus.

642 ***Fluorescent Recovery After Photobleaching and variance analysis***

643 Murine ES cells transfected with HP1α-GFP were harvested with trypsin (Gibco) and plated
644 for 4-6h onto 0.1% gelatin-coated glass live-cell Nunc slides (Thermo). FRAP experiment was
645 carried with an LSM 800 confocal microscope (Zeiss). The 488nm laser was used to bleach
646 and acquire GFP signal. 1 image was taken before a bleach pulse of 5ms. Bleaching area was
647 set to target a single pericentric domain. Images were acquired every second during 35s post-
648 bleach. FRAP analysis was performed using a FRAP analysis ImageJ Jython script, that
649 generated FRAP curves and the associated half-recovery time and mobile fraction parameters.

650 GFP-HP1α variance along time was obtained from ImageJ analysis using standard deviation
651 z-projection along time for the whole duration of the movie. Quantification of heterochromatin
652 barriers were performed using a 1µm line across individual non-bleached chromocenter
653 borders, for which the variance intensity along time was measured with the ImageJ software.

654 ***Image acquisition and analysis***

655 Images for immunofluorescence and FISH experiments were obtained with an inverted Nikon
656 Ti Eclipse widefield microscope using a 60X immersion objective and LED sources. Z-stacks
657 images were taken and then deconvoluted using a custom ImageJ deconvolution script.
658 Quantifications of images were performed using custom Icy scripts in Icy and ImageJ. To
659 quantify DAXX enrichment at PCH and the number of PCH foci, chromocenters were
660 segmented using ICY the spot detector function on either H3K9me3 or major satellite FISH
661 signal. Nuclei were isolated using the ICY k-means segmentation script. The nuclear periphery
662 enrichment was measured in ImageJ, briefly linescans of LaminB1 and H3K9me2 at the

663 periphery were isolated using the straighten command and subsequently used to generated
664 intensity profiles.

665 H3K9me3 intensities at chromocenters were measured using à 2µm line across individual
666 DAPI-dense chromocenters. Two to three chromocenters per nucleus were analyzed.

667 ***Statistical analysis***

668 Number of objects counted, and statistical tests performed are indicated in the text, figure or
669 figure legends. All statistical analysis results are listed in supplementary file. Pvalues are
670 represented as follow: * <0.05; **<0.01; ***<0.001; ****<0.0001.

671 ***Western Blotting***

672 Total protein extracts were prepared in RIPA buffer with protease inhibitor cocktail (Roche).
673 Samples were sonicated for 3 minutes alterning 30seconds ON/ 30seconds OFF. Proteins
674 were separated by electrophoresis in 8-15% poly-acrylamide gels then transferred onto
675 nitrocellulose membranes. Membranes were incubated in ponceau then washed in PBS, 0.1%
676 tween. Membranes were blocked in PBS, 0.1% tween, 5% milk for 30min at room temperature
677 before incubation with primary antibody overnight at 4°C. After 3 washed in PBS, 0.1% tween,
678 membranes were incubated with secondary HRP-conjugated antibody for 1h at room
679 temperature. Membranes were washed 3 times in PBS, 0.1% tween and visualized by
680 chemoluminescence using ECL Plus.

681

682 **Acknowledgements**

683 We would like to thank A. Bonnet-Garnier and A. Jouneau for the gift of Suv39dKO KO
684 ESCs and advice. We are also grateful to image core microscopy facilities of IRSL, Paris, in
685 particular N. Setterblad for his assistance with live imaging. We warmly thank V. Lallemand-
686 Breitenbach and H. de Thé (Collège de France, Paris, France) for the sharing of PML antibody
687 and helpful advice. We are thankful to Y. Khalil for her help in microscopy analysis. We kindly

thank P. Lesage and Annia Carré Simon for their critical readings of the manuscript, and other members of the team for helpful advice. We finally thank support services of IRSL. This work was funded by Agence Nationale pour la Recherche (ANR-16-CE12-0003), IDEX SLI, La Ligue Nationale Contre le Cancer (LNCC)-Comité Ile de France and the labex Who am I. AC was supported by MESR and LNCC. The authors declare no conflict of interest.

Author Contributions

AC, AV, CD, PT, performed all experiments, RI analyzed RNAseq data. AC, AV, PT designed experiments, interpreted data. RB wrote the scripts for image analysis. AC, EF, PT contributed to the writing of the manuscript. All authors reviewed the manuscript.

Declaration of interest

The authors declare no competing interests.

References

Adam, S., Polo, S. E. and Almouzni, G. (2013). Transcription recovery after DNA damage requires chromatin priming by the H3.3 histone chaperone HIRA. *Cell* 155, 94–106.

Aloia, L., Stefano, B. D. and Croce, L. D. (2013). Polycomb complexes in stem cells and embryonic development. *Development* 140, 2525–2534.

Arakawa, T., Nakatani, T., Oda, M., Kimura, Y., Sekita, Y., Kimura, T., Nakamura, T. and Nakano, T. (2015). Stella controls chromocenter formation through regulation of Daxx expression in 2-cell embryos. *Biochemical and biophysical research communications* 466, 60–65.

Blaschke, K., Ebata, K. T., Karimi, M. M., Zepeda-Martínez, J. A., Goyal, P., Mahapatra, S., Tam, A., Laird, D. J., Hirst, M., Rao, A., et al. (2013). Vitamin C induces Tet-dependent DNA demethylation and a blastocyst-like state in ES cells. *Nature* 500, 222–226.

Borgel, J., Guibert, S., Li, Y., Chiba, H., Schübeler, D., Sasaki, H., Forné, T. and Weber, M. (2010). Targets and dynamics of promoter DNA methylation during early mouse development. *Nature Genetics* 42, 1093–1100.

717 Burton, A. and Torres-Padilla, M.-E. (2014). Chromatin dynamics in the regulation of cell fate allocation
718 during early embryogenesis. *Nat Rev Mol Cell Bio* 15, 723–735.

719 Buschbeck, M. and Hake, S. B. (2017). Variants of core histones and their roles in cell fate decisions,
720 development and cancer. *Nature Reviews Molecular Cell Biology* 18, 299–314.

721 Casanova, M., Pasternak, M., Marjou, F. E., Baccon, P. L., Probst, A. V. and Almouzni, G. (2013).
722 Heterochromatin reorganization during early mouse development requires a single-stranded
723 noncoding transcript. *Cell reports* 4, 1156–1167.

724 Cho, S., Park, J. S. and Kang, Y.-K. (2011). Dual functions of histone-lysine N-methyltransferase Setdb1
725 protein at promyelocytic leukemia-nuclear body (PML-NB): maintaining PML-NB structure and
726 regulating the expression of its associated genes. *Journal of Biological Chemistry* 286, 41115–
727 41124.

728 Cho, S., Park, J. S., Kwon, S. and Kang, Y.-K. (2012). Dynamics of Setdb1 expression in early mouse
729 development. *Gene expression patterns : GEP* 12, 213–218.

730 Consortium, M. G. S., Waterston, R. H., Lindblad-Toh, K., Birney, E., Rogers, J., Abril, J. F., Agarwal, P.,
731 Agarwala, R., Ainscough, R., Alexandersson, M., et al. (2002). Initial sequencing and comparative
732 analysis of the mouse genome. *Nature* 420, 520–562.

733 Crosetto, N., Mitra, A., Silva, M. J., Bienko, M., Dojer, N., Wang, Q., Karaca, E., Chiarle, R., Skrzypczak,
734 M., Ginalski, K., et al. (2013). Nucleotide-resolution DNA double-strand break mapping by next-
735 generation sequencing. *Nature methods* 10, 361–365.

736 Delbarre, E., Ivanauskiene, K., Küntziger, T. and Collas, P. (2013). DAXX-dependent supply of soluble
737 (H3.3-H4) dimers to PML bodies pending deposition into chromatin. *Genome Research* 23, 440–
738 451.

739 Delbarre, E., Ivanauskiene, K., Spirkoski, J., Shah, A., Vekterud, K., Moskaug, J. Ø., Bøe, S. O., Wong, L.
740 H., Küntziger, T. and Collas, P. (2017). PML protein organizes heterochromatin domains where it
741 regulates histone H3.3 deposition by ATRX/DAXX. *Genome Research* 27, 913–921.

742 Ding, Q., Lee, Y.-K., Schaefer, E. A. K., Peters, D. T., Veres, A., Kim, K., Kuperwasser, N., Motola, D. L.,
743 Meissner, T. B., Hendriks, W. T., et al. (2013). A TALEN genome-editing system for generating
744 human stem cell-based disease models. *Cell stem cell* 12, 238–251.

745 Drané, P., Ouararhni, K., Depaux, A., Shuaib, M. and Hamiche, A. (2010). The death-associated protein
746 DAXX is a novel histone chaperone involved in the replication-independent deposition of H3.3.
747 *Genes & Development* 24, 1253–1265.

748 Elsässer, S. J., Huang, H., Lewis, P. W., Chin, J. W., Allis, C. D. and Patel, D. J. (2012). DAXX envelops a
749 histone H3.3-H4 dimer for H3.3-specific recognition. *Nature* 491, 560–565.

750 Elsässer, S. J., Noh, K.-M., Diaz, N., Allis, C. D. and Banaszynski, L. A. (2015). Histone H3.3 is required for
751 endogenous retroviral element silencing in embryonic stem cells. *Nature* 522, 240–244.

752 Escobar-Cabrera, E., Lau, D. K. W., Giovinazzi, S., Ishov, A. M. and McIntosh, L. P. (2010). Structural
753 characterization of the DAXX N-terminal helical bundle domain and its complex with Rassf1C.
754 *Structure (London, England : 1993)* 18, 1642–1653.

755 Falk, M., Feodorova, Y., Naumova, N., Imakaev, M., Lajoie, B. R., Leonhardt, H., Joffe, B., Dekker, J.,
756 Fudenberg, G., Solovei, I., et al. (2019). Heterochromatin drives compartmentalization of inverted
757 and conventional nuclei. *Nature* 40, 47.

758 Fortuny, A., Chansard, A., Caron, P., Chevallier, O., Leroy, O., Renaud, O. and Polo, S. E. (2021). Imaging
759 the response to DNA damage in heterochromatin domains reveals core principles of
760 heterochromatin maintenance. *Nature communications* 12, 2428–16.

761 Fukuda, K., Okuda, A., Yusa, K. and Shinkai, Y. (2018). A CRISPR knockout screen identifies SETDB1-
762 target retroelement silencing factors in embryonic stem cells. *Genome Research* 28, 846–858.

763 Gauchier, M., Kan, S., Barral, A., Sauzet, S., Agirre, E., Bonnell, E., Saksouk, N., Barth, T. K., Ide, S.,
764 Urbach, S., et al. (2019). SETDB1-dependent heterochromatin stimulates alternative lengthening of
765 telomeres. *Science advances* 5, eaav3673.

766 Guelen, L., Pagie, L., Brasset, E., Meuleman, W., Faza, M. B., Talhout, W., Eussen, B. H., Klein, A. de,
767 Wessels, L., Laat, W. de, et al. (2008). Domain organization of human chromosomes revealed by
768 mapping of nuclear lamina interactions. *Nature* 453, 948–951.

769 Guenatri, M., Bailly, D., Maison, C. and Almouzni, G. (2004). Mouse centric and pericentric satellite
770 repeats form distinct functional heterochromatin. *The Journal of cell biology* 166, 493–505.

771 Hahn, M., Dambacher, S., Dulev, S., Kuznetsova, A. Y., Eck, S., Wörz, S., Sadic, D., Schulte, M., Mallm,
772 J.-P., Maiser, A., et al. (2013). Suv4-20h2 mediates chromatin compaction and is important for
773 cohesin recruitment to heterochromatin. *Genes & Development* 27, 859–872.

774 He, Q., Kim, H., Huang, R., Lu, W., Tang, M., Shi, F., Yang, D., Zhang, X., Huang, J., Liu, D., et al. (2015).
775 The Daxx/Atrx Complex Protects Tandem Repetitive Elements during DNA Hypomethylation by
776 Promoting H3K9 Trimethylation. *Cell stem cell* 17, 273–286.

777 Healton, S. E., Pinto, H. D., Mishra, L. N., Hamilton, G. A., Wheat, J. C., Swist-Rosowska, K., Shukeir, N.,
778 Dou, Y., Steidl, U., Jenuwein, T., et al. (2020). H1 linker histones silence repetitive elements by
779 promoting both histone H3K9 methylation and chromatin compaction. *Proceedings of the National*
780 *Academy of Sciences of the United States of America* 117, 14251–14258.

781 Hinde, E., Cardarelli, F. and Gratton, E. (2015). Spatiotemporal regulation of Heterochromatin Protein
782 1-alpha oligomerization and dynamics in live cells. *Scientific reports* 5, 12001–11.

783 Hoelper, D., Huang, H., Jain, A. Y., Patel, D. J. and Lewis, P. W. (2017). Structural and mechanistic
784 insights into ATRX-dependent and -independent functions of the histone chaperone DAXX. *Nature*
785 *communications* 8, 1193.

786 Jachowicz, J. W., Bing, X., Pontabry, J., Bošković, A., Rando, O. J. and Torres-Padilla, M.-E. (2017). LINE-
787 1 activation after fertilization regulates global chromatin accessibility in the early mouse embryo.
788 *Nature Genetics* 11, 778.

789 Jagannathan, M., Cummings, R. and Yamashita, Y. M. (2018). A conserved function for pericentromeric
790 satellite DNA. *eLife* 7, 1218.

791 Jang, C.-W., Shibata, Y., Starmer, J., Yee, D. and Magnuson, T. (2015). Histone H3.3 maintains genome
792 integrity during mammalian development. *Genes & Development* 29, 1377–1392.

793 Juhász, S., Elbakry, A., Mathes, A. and Löbrich, M. (2018). ATRX Promotes DNA Repair Synthesis and
794 Sister Chromatid Exchange during Homologous Recombination. *Molecular Cell* 71, 11-24.e7.

795 Jurkowska, R. Z., Qin, S., Kungulovski, G., Tempel, W., Liu, Y., Bashtrykov, P., Stiefelmaier, J., Jurkowski,
796 T. P., Kudithipudi, S., Weirich, S., et al. (2017). H3K14ac is linked to methylation of H3K9 by the
797 triple Tudor domain of SETDB1. *Nature communications* 8, 2057.

798 Karimi, M. M., Goyal, P., Maksakova, I. A., Bilenky, M., Leung, D., Tang, J. X., Shinkai, Y., Mager, D. L.,
799 Jones, S., Hirst, M., et al. (2011). DNA methylation and SETDB1/H3K9me3 regulate predominantly
800 distinct sets of genes, retroelements, and chimeric transcripts in mESCs. 8, 676–687.

801 Kind, J., Pagie, L., Ortabozkoyun, H., Boyle, S., Vries, S. S. de, Janssen, H., Amendola, M., Nolen, L. D.,
802 Bickmore, W. A. and Steensel, B. van (2013). Single-cell dynamics of genome-nuclear lamina
803 interactions. *Cell* 153, 178–192.

804 Koningsbruggen, S. van, Gierlinski, M., Schofield, P., Martin, D., Barton, G. J., Ariyurek, Y., Dunnen, J. T.
805 den and Lamond, A. I. (2010). High-resolution whole-genome sequencing reveals that specific
806 chromatin domains from most human chromosomes associate with nucleoli. *Molecular biology of*
807 *the cell* 21, 3735–3748.

808 Lallemand-Breitenbach, V. and Thé, H. de (2018). PML nuclear bodies: from architecture to function.
809 *Current Opinion in Cell Biology* 52, 154–161.

810 Larson, A. G., Elnatan, D., Keenen, M. M., Trnka, M. J., Johnston, J. B., Burlingame, A. L., Agard, D. A.,
811 Redding, S. and Narlikar, G. J. (2017). Liquid droplet formation by HP1α suggests a role for phase
812 separation in heterochromatin. *Nature* 547, 236–240.

813 Lehnertz, B., Ueda, Y., Derijck, A. A. H. A., Braunschweig, U., Perez-Burgos, L., Kubicek, S., Chen, T., Li,
814 E., Jenuwein, T. and Peters, A. H. F. M. (2003). Suv39h-mediated histone H3 lysine 9 methylation
815 directs DNA methylation to major satellite repeats at pericentric heterochromatin. *Current Biology*
816 13, 1192–1200.

817 Leitch, H. G., McEwen, K. R., Turp, A., Encheva, V., Carroll, T., Grabole, N., Mansfield, W., Nashun, B.,
818 Knezovich, J. G., Smith, A., et al. (2013). Naive pluripotency is associated with global DNA
819 hypomethylation. *Nature structural & molecular biology* 20, 1–9.

820 Lewis, P. W., Elsaesser, S. J., Noh, K.-M., Stadler, S. C. and Allis, C. D. (2010). Daxx is an H3.3-specific
821 histone chaperone and cooperates with ATRX in replication-independent chromatin assembly at
822 telomeres. *Proceedings of the National Academy of Sciences of the United States of America* 107,
823 14075–14080.

824 Li, X. and Tyler, J. K. (2016). Nucleosome disassembly during human non-homologous end joining
825 followed by concerted HIRA- and CAF-1-dependent reassembly. *eLife* 5, 94.

826 Lin, C.-J., Conti, M. and Ramalho-Santos, M. (2013). Histone variant H3.3 maintains a decondensed
827 chromatin state essential for mouse preimplantation development. *Development* 140, 3624–3634.

828 Liu, Z., Tardat, M., Gill, M. E., Royo, H., Thierry, R., Ozonov, E. A. and Peters, A. H. (2020). SUMOylated
829 PRC1 controls histone H3.3 deposition and genome integrity of embryonic heterochromatin. *The*
830 *EMBO Journal* e103697.

831 Loyola, A., Tagami, H., Bonaldi, T., Roche, D., Quivy, J.-P., Imhof, A., Nakatani, Y., Dent, S. Y. R. and
832 Almouzni, G. (2009). The HP1alpha-CAF1-SetDB1-containing complex provides H3K9me1 for Suv39-
833 mediated K9me3 in pericentric heterochromatin. *EMBO reports* 10, 769–775.

834 Lu, J. Y., Chang, L., Li, T., Wang, T., Yin, Y., Zhan, G., Han, X., Zhang, K., Tao, Y., Percharde, M., et al.
835 (2021). Homotypic clustering of L1 and B1/Alu repeats compartmentalizes the 3D genome. *Cell*
836 *research* 1, 26.

837 Luciani, J. J., Depetris, D., Usson, Y., Metzler-Guillemain, C., Mignon-Ravix, C., Mitchell, M. J.,
838 Megarbane, A., Sarda, P., Sirma, H., Moncla, A., et al. (2006). PML nuclear bodies are highly
839 organised DNA-protein structures with a function in heterochromatin remodelling at the G2 phase.
840 *Journal of Cell Science* 119, 2518–2531.

841 Luijsterburg, M. S., Krijger, I. de, Wiegant, W. W., Shah, R. G., Smeenk, G., Groot, A. J. L. de, Pines, A.,
842 Vertegaal, A. C. O., Jacobs, J. J. L., Shah, G. M., et al. (2016). PARP1 Links CHD2-Mediated Chromatin
843 Expansion and H3.3 Deposition to DNA Repair by Non-homologous End-Joining. *Molecular Cell* 61,
844 547–562.

845 Mansuroglu, Z., Benhelli-Mokrani, H., Marcato, V., Sultan, A., Violet, M., Chauderlier, A., Delattre, L.,
846 Loyens, A., Talahari, S., Bégard, S., et al. (2016). Loss of Tau protein affects the structure,
847 transcription and repair of neuronal pericentromeric heterochromatin. *Scientific reports* 6, 33047.

848 Martens, J. H. A., O'Sullivan, R. J., Braunschweig, U., Opravil, S., Radolf, M., Steinlein, P. and Jenuwein,
849 T. (2005). The profile of repeat-associated histone lysine methylation states in the mouse
850 epigenome. *The EMBO Journal* 24, 800–812.

851 Matsui, T., Leung, D., Miyashita, H., Maksakova, I. A., Miyachi, H., Kimura, H., Tachibana, M., Lorincz,
852 M. C. and Shinkai, Y. (2010). Proviral silencing in embryonic stem cells requires the histone
853 methyltransferase ESET. *Nature* 464, 927–931.

854 Mendiratta, S., Gatto, A. and Almouzni, G. (2019). Histone supply: Multitiered regulation ensures
855 chromatin dynamics throughout the cell cycle. *J Cell Biol* 218, 39–54.

856 Michaelson, J. S., Bader, D., Kuo, F., Kozak, C. and Leder, P. (1999). Loss of Daxx, a promiscuously
857 interacting protein, results in extensive apoptosis in early mouse development. *Genes &*
858 *Development* 13, 1918–1923.

859 Miyanari, Y., Ziegler-Birling, C. and Torres-Padilla, M.-E. (2013). Live visualization of chromatin
860 dynamics with fluorescent TALEs. *Nat Biotechnology* 20, 1321–1324.

861 Nakatani, T., Yamagata, K., Kimura, T., Oda, M., Nakashima, H., Hori, M., Sekita, Y., Arakawa, T.,
862 Nakamura, T. and Nakano, T. (2015). Stella preserves maternal chromosome integrity by inhibiting
863 5hmC-induced γH2AX accumulation. *EMBO reports* 16, 582–589.

864 Pailles, M., Hirlemann, M., Brochard, V., Chebrout, M., Oudin, J.-F., Marks, H., Jouneau, A. and Bonnet-
865 Garnier, A. (2022). H3K27me3 at pericentromeric heterochromatin is a defining feature of the early
866 mouse blastocyst. *Sci Rep-uk* 12, 13908.

867 Park, J., Lee, H., Han, N., Kwak, S., Lee, H.-T., Kim, J.-H., Kang, K., Youn, B. H., Yang, J.-H., Jeong, H.-J., et
868 al. (2018). Long non-coding RNA ChRO1 facilitates ATRX/DAXX-dependent H3.3 deposition for
869 transcription-associated heterochromatin reorganization. *Nucleic acids research* 46, 11759–11775.

870 Peric-Hupkes, D., Meuleman, W., Pagie, L., Bruggeman, S. W. M., Solovei, I., Brugman, W., Gräf, S.,
871 Flicek, P., Kerkhoven, R. M., Lohuizen, M. van, et al. (2010). Molecular maps of the reorganization
872 of genome-nuclear lamina interactions during differentiation. *Molecular Cell* 38, 603–613.

873 Peters, A. H., O'Carroll, D., Scherthan, H., Mechtler, K., Sauer, S., Schöfer, C., Weipoltshammer, K.,
874 Pagani, M., Lachner, M., Kohlmaier, A., et al. (2001). Loss of the Suv39h histone methyltransferases
875 impairs mammalian heterochromatin and genome stability. *Cell* 107, 323–337.

876 Pinheiro, I., Margueron, R., Shukeir, N., Eisold, M., Fritzsch, C., Richter, F. M., Mittler, G., Genoud, C.,
877 Goyama, S., Kurokawa, M., et al. (2012). Prdm3 and Prdm16 are H3K9me1 methyltransferases
878 required for mammalian heterochromatin integrity. *Cell* 150, 948–960.

879 Probst, A. V., Okamoto, I., Casanova, M., Marjou, F. E., Baccon, P. L. and Almouzni, G. (2010). A strand-
880 specific burst in transcription of pericentric satellites is required for chromocenter formation and
881 early mouse development. *Developmental Cell* 19, 625–638.

882 Ran, F. A., Hsu, P. D., Wright, J., Agarwala, V., Scott, D. A. and Zhang, F. (2013). Genome engineering
883 using the CRISPR-Cas9 system. *Nature protocols* 8, 2281–2308.

884 Sadic, D., Schmidt, K., Groh, S., Kondofersky, I., Ellwart, J., Fuchs, C., Theis, F. J. and Schotta, G. (2015).
885 Atrx promotes heterochromatin formation at retrotransposons. *EMBO reports* 16, 836–850.

886 Saksouk, N., Barth, T. K., Ziegler-Birling, C., Olova, N., Nowak, A., Rey, E., Mateos-Langerak, J., Urbach,
887 S., Reik, W., Torres-Padilla, M.-E., et al. (2014). Redundant mechanisms to form silent chromatin at
888 pericentromeric regions rely on BEND3 and DNA methylation. *Molecular Cell* 56, 580–594.

889 Salsman, J., Rapkin, L. M., Margam, N. N., Duncan, R., Bazett-Jones, D. P. and Dellaire, G. (2017).
890 Myogenic differentiation triggers PML nuclear body loss and DAXX relocalization to chromocentres.
891 *Cell death & disease* 8, e2724.

892 Song, Y. J., Choi, J. H. and Lee, H. (2015). Setdb1 is required for myogenic differentiation of C2C12
893 myoblast cells via maintenance of MyoD expression. *Molecules and cells* 38, 362–372.

894 Strom, A. R., Emelyanov, A. V., Mir, M., Fyodorov, D. V., Darzacq, X. and Karpen, G. H. (2017). Phase
895 separation drives heterochromatin domain formation. *Nature* 547, 241–245.

896 Szenker, E., Ray-Gallet, D. and Almouzni, G. (2011). The double face of the histone variant H3.3. *Cell*
897 *research* 21, 421–434.

898 Tessier, S., Ferhi, O., Geoffroy, M.-C., González-Prieto, R., Canat, A., Quentin, S., Pla, M., Niwa-
899 Kawakita, M., Bercier, P., Rérolle, D., et al. (2022). Exploration of nuclear body-enhanced
900 sumoylation reveals that PML represses 2-cell features of embryonic stem cells. *Nat Commun* 13,
901 5726.

902 Therizols, P., Illingworth, R. S., Courilleau, C., Boyle, S., Wood, A. J. and Bickmore, W. A. (2014).
903 Chromatin decondensation is sufficient to alter nuclear organization in embryonic stem cells.
904 *Science* 346, 1238–1242.

905 Tosolini, M., Brochard, V., Adenot, P., Chebrout, M., Grillo, G., Navia, V., Beaujean, N., Francastel, C.,
906 Bonnet-Garnier, A. and Jouneau, A. (2018). Contrasting epigenetic states of heterochromatin in the
907 different types of mouse pluripotent stem cells. *Scientific reports* 8, 5776.

908 Walter, M., Teissandier, A., Pérez-Palacios, R. and Bourc'his, D. (2016). An epigenetic switch ensures
909 transposon repression upon dynamic loss of DNA methylation in embryonic stem cells. *eLife* 5, R87.

910 Wang, L., Gao, Y., Zheng, X., Liu, C., Dong, S., Li, R., Zhang, G., Wei, Y., Qu, H., Li, Y., et al. (2019). Histone
911 Modifications Regulate Chromatin Compartmentalization by Contributing to a Phase Separation
912 Mechanism. *Molecular Cell* 76, 646-659.e6.

913 Wijchers, P. J., Geeven, G., Eyres, M., Bergsma, A. J., Janssen, M., Verstegen, M., Zhu, Y., Schell, Y.,
914 Vermeulen, C., Wit, E. de, et al. (2015). Characterization and dynamics of pericentromere-
915 associated domains in mice. *Genome Research* 25, 958–969.

916 Wossidlo, M., Nakamura, T., Lepikhov, K., Marques, C. J., Zakhartchenko, V., Boiani, M., Arand, J.,
917 Nakano, T., Reik, W. and Walter, J. (2011). 5-Hydroxymethylcytosine in the mammalian zygote is
918 linked with epigenetic reprogramming. *Nature communications* 2, 241.

919 Ying, Q.-L., Wray, J., Nichols, J., Batlle-Morera, L., Doble, B., Woodgett, J., Cohen, P. and Smith, A.
920 (2008). The ground state of embryonic stem cell self-renewal. *Nature* 453, 519–523.

921 Zhu, Q., Pao, G. M., Huynh, A. M., Suh, H., Tonnu, N., Nederlof, P. M., Gage, F. H. and Verma, I. M.
922 (2011). BRCA1 tumour suppression occurs via heterochromatin-mediated silencing. *Nature* 477,
923 179–184.

924 Ziegler-Birling, C., Helmrich, A., Tora, L. and Torres-Padilla, M.-E. (2009). Distribution of p53 binding
925 protein 1 (53BP1) and phosphorylated H2A.X during mouse preimplantation development in the
926 absence of DNA damage. *The International journal of developmental biology* 53, 1003–1011.

927

928

929 **Legends**

930 **Legends**

931 **Fig. 1 | DAXX is essential for ESC survival upon ground-state conversion and is required**
932 **for transcriptional repression of peripheral heterochromatin. (A)** Schematic of the *Daxx*
933 locus and the of the guide RNA targeting exon 3. Left, RT-qPCR experiment on DAXX RNA in
934 WT cells or cells after CrispR/cas9 editing on *Daxx*. The mean of two biological replicates with
935 SEM are shown. Right, western blot with anti-DAXX antibody, anti-LAMIN-B1 and anti-H3.3
936 served as loading control. One experiment from at least 2 biological replicates is shown. **(B)**
937 Quantification of the number of cells (in %) compared to WT in each culture condition, serum,
938 after 4 days (4d) or 8 days (8d) of 2iV conversion and after 5 days of Retinoic Acid
939 differentiation (Diff.) Histogram represents mean with SEM of 3 biological replicates for each
940 condition except Diff. (mean of two biological replicates). T-tests were used for statistical
941 analysis. **(C)** RNA-seq tracks of 2 Lamin Associated Domains (LAD) of WT ESCs (blue) and
942 *Daxx* KO (orange) under serum and 2iV conditions. **(D)** Boxplots of the log2 fold change of
943 mRNA levels of genes located in LAD (LAD, orange) and non-LAD (CEN, blue) regions in *Daxx*
944 KO over WT ESCs, grown in 2iV, serum and diff. media. Two-sided Mann-Whitney tests was
945 used for statistical analysis **(E)** Representative nuclei after immuno-detection of H3K9me2
946 (red) and counterstaining with DAPI (blue) in WT and *Daxx* KO ESCs in serum and 2iV (scale
947 bar = 2µm). Linescans below represent straighten H3K9me2 signal at the nuclear periphery
948 (black). **(E)** Boxplots of H3K9me2 signal quantification enrichment at the nuclear periphery
949 from 2 independent replicates. Two-sided Mann-Whitney tests was used for statistical analysis.

950 **Fig. 2 | DAXX is recruited to PCH in 2iV converted ESCs. (A)** Heatmap for different classes
951 of transposable elements. Data are mean from RNA-seq experiments on 3 biological
952 replicates. **(B)** Representative nuclei of ESCs grown in serum or 2iV immuno-detected with
953 H3K9me3 (red) and DAXX (green). Nuclei were counterstained with DAPI (cyan). Scale bar =
954 2µm. **(C)** Boxplot of mean DAXX levels at pericentromeric heterochromatin (PCH) in WT ESCs
955 grown in serum (white) or in 2iV (red) from 3 biological replicates. **(D)** Distribution curve of
956 DAXX intensity observed at individual PCH foci in WT ESCs grown in serum (white) or in 2iV

957 (red) from 3 independent replicates. Dashed line indicates the threshold used to defined DAXX-
958 positive PCH. **(E)** Histogram of the average fraction of the cell population with 0, 1, 2 and 3 or
959 more, DAXX-positive PCH foci in WT ESCs in serum and 2iV. SEM are shown. **(F)** Boxplots
960 of DAXX-negative (neg) and DAXX-positive (pos) PCH foci surface in WT ESCs grown in
961 serum (white) or in 2iV (red). **(G)** Boxplots of H3K9me3 intensity in DAXX-negative (neg) and
962 DAXX-positive (pos) PCH foci in WT ESCs grown in serum (white) or in 2iV (red). Mann-
963 Whitney tests were used for statistical analysis in C, F and G.

964 **Fig. 3 | DAXX maintains heterochromatin organization in pluripotent cells. (A)**
965 Representative major satellite (MajSat) DNA FISH pictures of WT and Daxx KO ESCs in
966 serum, 2iV and differentiation (Diff.) conditions. **(B)** Quantification of the number of major
967 satellite foci per nucleus in WT (blue) or *Daxx* KO (yellow) ESC. n=total number of nuclei
968 analyzed from at least 3 biological replicates. **(C)** Representative immunoFISH pictures of
969 major satellite and Flag for *Daxx* KO cells transfected with $TALE_{MajSat}$-Δ or $TALE_{MajSat}$-DAXX.
970 **(D)** Quantification of the number of major satellite foci detected in the focal plane. n= total
971 number of nuclei analyzed from 4 biological replicates. **(E)** Top, scheme depicting the two
972 different analyses used in live-imaging experiments. Bottom, representative pictures from
973 FRAP experiments performed on WT and *Daxx* KO cells transfected with GFP-HP1α. t=-5''
974 corresponds to pre-bleach fluorescence. t=0 corresponds to the laser bleach pulse. t=4'' and
975 t=23'' correspond to post-bleach recovery images after 4 and 23 seconds respectively. **(F)**
976 Quantification of half-recovery times in seconds for individual nuclei. n=total number of nuclei
977 analyzed from 2 biological replicates. **(G)** Representative pictures of GFP-HP1α and its
978 corresponding variance in fluorescence intensities along time in serum or 2iV, WT or *Daxx* KO
979 ESCs. White dashed squares display magnification of individual chromocenters. Color
980 correspondence of signal variance strength (from high to low) is shown. Scale bar, 5μm. **(H)**
981 Graph displaying the variance intensities along measured on 1μm lines traced above non-
982 bleached foci. Two-sided Mann-Whitney tests were used for statistical analysis in B, D and F.

983 **Fig. 4 | PML protects heterochromatin in ground-state ESCs. (A)** Representative field of
984 WT ESCs grown in serum or 2iV immuno-detection of H3K9me3 (red), PML (green), DAXX
985 (purple) and counterstaining with DAPI (cyan). White squares highlight the absence (serum)
986 or the presence (2iV) of PML-rim around H3K9me3 foci. **(B)** Histogram of the average fraction
987 of cell population showing either 0, 1, 2 and 3 or more, PML-rims, with SEM, in 2i converted
988 WT ESCs (n= total number of nuclei). **(C)** Representative major satellite DNA FISH pictures of
989 *Pml* KO ESCs in serum, 2iV and differentiation (dif.) conditions. **(D)** Quantification of the
990 number of major satellite foci per nucleus. WT values (blue) are taken from Fig. 3B. n=total
991 number of nuclei analyzed from at least 3 biological replicates. **(E)** Representative nuclei
992 immuno-detection of H3K9me2 (red) and counterstaining with DAPI (blue) in *Pml* KO ESCs
993 grown in serum and 2iV (scale bar = 2µm). Linescan represent straighten H3K9me3 signal at
994 the nuclear periphery (black). **(F)** Boxplots of H3K9me2 signal quantification enrichment at the
995 nuclear periphery. WT values (blue) are taken from Fig. 1F. n=total number of nuclei analyzed
996 from at least 3 biological replicates. **(G)** RT-qPCR RNA quantification of LAD genes in WT and
997 *Pml* KO ESCs in serum and upon 2iV conversion. Histogram represents means normalized to
998 WT-serum with SEM of 3 biological replicates. T-tests were used for statistical analysis **(H)**
999 Quantification of the number of cells compared to WT in each culture condition. Histogram
1000 represents mean with SEM of 3 biological replicates. Two-sided Mann-Whitney tests were
1001 used for statistical analysis in D and F.

1002 **Fig. 5 | DAXX recruits Setdb1 and mediates chromocenter clustering via H3.3K9me3**
1003 **modification. (A)** Representative immunofluorescence pictures for SETDB1, DAXX and PML
1004 in WT or *Daxx* KO ESCs upon 2iV conversion. **(B)** Quantification of the mean number of PML
1005 or SETDB1 foci at chromocenters in WT and *Daxx* KO ESCs. n= total number of nuclei
1006 analyzed from two independent replicates. Chi-square tests were used for statistical analysis.
1007 **(C)** Representative immunoFISH pictures for H3K9me3, PML and major satellites in 2iV and
1008 serum of Suv39H1/2 dKO (double knock out) ESCs. White dashed squares highlight a major
1009 satellite focus. **(D)** Cumulated fluorescence intensities profile of H3K9me3 positive PCH foci in

1010 cells grown in serum or 2iV for either H3K9me3, PCH or PML signal. n=total number of nuclei
1011 analyzed from at least 2 biological replicates. **(E)** Representative immunofluorescence pictures
1012 for H3K9me3 and Flag in Suv39dKO serum ESCs transfected with $TALE_{MajSat}$-Δ, $TALE_{MajSat}$-
1013 SUV39H1, $TALE_{MajSat}$-SETDB1, $TALE_{MajSat}$-DAXX or $TALE_{MajSat}$-$DAXX^{Y222A}$. **(F)** quantification
1014 of the number of PCH foci observed in the different transfection conditions described in E. **(G)**
1015 Representative immunoFISH pictures for major satellite and Flag in *Daxx* KO serum ESCs co-
1016 transfected with siRNA against H3.3, $TALE_{MajSat}$-DAXX and either no additional construct or
1017 H3.3WT, H3.3G90M or H3.3K9A. **(H)** Quantification of the number of major satellite foci
1018 detected of medium focal plane observed in the different transfection conditions described in
1019 G. For comparison, distribution T_{MS}-DAXX without H3.3 knockdown data comes from Fig. 3D.
1020 n=total number of nuclei analyzed from 2 biological replicates. Two-sided Mann-Whitney tests
1021 were used for statistical analysis in F and H.

1022 **Fig. 6 | Model for heterochromatin maintenance by DAXX in ESCs.**

1023 During ground-state conversion of ESCs, DAXX accumulates at PCH and is surrounded by a
1024 PML shell. DAXX recruits the histone methyltransferase SETDB1 to promote H3.3K9me3 to
1025 maintain the pericentromeric heterochromatin. In *Daxx* and *Pml* KO cells, the 3D-organization
1026 of heterochromatin is impaired. The peripheral heterochromatin H3K9me2 fails to accumulate
1027 properly at the nuclear edge leading to promiscuous expression of genes located in LADs. The
1028 clustering and the physical properties of pericentromeric heterochromatin is impacted,
1029 impairing transcriptional repression of major satellites. The global defect of heterochromatin
1030 observed in these cells prevents prolonged culture of these cells in ground-state condition.

1031

1032 ## Supplemental material legends

1033 **Fig. S1 | Impact of *Daxx* deletion on ground-state conversion. (A)** Representative field of
1034 WT and *Daxx* KO ESCs after IF against DAXX (green) and counterstaining with DAPI (cyan).
1035 Scale bar = 5µm. **(B)** Dot blot using 5mC antibody to assess global DNA methylation levels
1036 upon 2iV conversion. One experiment is shown. Histogram displays mean with SEM from 3

1037 independent replicates. **(C)** Volcano plot representing the number of differentially expressed
1038 genes in ground-state, serum or differentiated cells from RNA-seq experiments as in C.
1039 Differentially expressed genes in red for down-regulated or blue for up-regulated correspond
1040 to Log2(FoldChange(KO/WT)) <-1 or >1 with p-value<0.05. **(D)** Heatmaps representing genes
1041 displaying strongest transcriptional changes upon 2iV conversion (left) or upon differentiation
1042 (right) normalized by transcription in serum conditions. Same set of genes for the *Daxx* KO
1043 ESCs. Data are from 3 biological replicates of RNA-seq experiments. **(E)** Volcano plots
1044 representing the number of differentially expressed genes upon 2iV conversion of WT and
1045 *Daxx* KO ESCs. Previously identified 2iV conversion markers are in red for up-regulated or
1046 blue for down-regulated (Blaschke et al., 2013).

1047 **Fig. S2 | Impact of *Daxx* deletion on nuclear periphery. (A)** RT-qPCR RNA quantification
1048 LAD genes in WT and *Daxx* KO ESCs in serum and upon 2iV conversion. Histogram
1049 represents mean normalized to WT-serum with SEM of 3 biological replicates. **(B)** Left,
1050 representative image of ESCs after IF against H3K9me2. Top right, linescan represents
1051 straighten H3K9me2 signal at the nuclear periphery (black). Bottom right, Intensity profiles of
1052 IF signals measured on linescans at the periphery (blue) or in the center (orange) of the
1053 nucleus. Ratio between mean intensity at the periphery and in the center was used to
1054 determined peripheral enrichment. **(C)** Representative nuclei after immuno-detection of
1055 LaminB1 (red) and counterstaining with DAPI (blue) in WT and *Daxx* KO ESCs in serum and
1056 2iV (scale bar = 2µm). Linescan represent straighten LaminB1 signal at the nuclear periphery
1057 (black). **(D)** Boxplots of LaminB1 signal quantification enrichment at the nuclear periphery from
1058 2 independent replicates. Mann-Whitney-tests were used for statistical analysis.

1059 **Fig. S3 | Impact of *Daxx* deletion on DNA repeats silencing.** RT-qPCR RNA quantification
1060 of DNA repeats. L1Tf , IAP elements and major satellites in WT and *Daxx* KO ESCs in serum,
1061 and upon differentiation or 2i+VitC (2iV) conversion. Histogram represents mean with SEM of
1062 3 biological replicates.

1063

1064 **Fig. S4 | Quantification of DAXX at chromocenters. (A)** Representative immunoFISH
1065 picture with H3K9me3 and major satellites DNA. **(B)** Dot plots of Pearson correlation between
1066 H3K9me3 and major satellite signals. **(C)** Representative field of ESCs grown in serum or 2iV
1067 immuno-detection of H3K9me3 (red), DAXX (green) and counterstaining with DAPI (cyan).
1068 White squares and arrows highlight the presence (2iV) of larger DAXX foci with higher levels
1069 of H3K9me3 and DAPI. Scale bar = 10µm. **(D)** Distribution of DAXX foci volume observed in
1070 WT ESCs grown in serum (black) or in 2iV (red) from 3 independent replicates. Dashed line
1071 indicates the threshold used to defined large or small DAXX foci. **(E)** Boxplots of DAPI signal
1072 intensity observed under small and large DAXX foci in serum (white) and 2iV (red) conditions.
1073 **(F)** Boxplots of H3K9me3 signal intensity observed under small and large DAXX foci in serum
1074 (white) and 2iV (red) conditions. **(G)** Top, ESCs nucleus after immuno-detection of H3K9me3,
1075 DAXX and counterstaining with DAPI. Bottom, for each nucleus, H3K9me3 and DAPI signals
1076 were segmented to PCH and nuclear ROIs. DAXX enrichment at PCH was defined by yhe
1077 ratio of DAXX intensity under PCH ROIs. Mann-Whitney-tests were used for statistical analysis
1078 in B, E and F.

1079 **Fig. S5 | Role of DAXX on pericentromeric heterochromatin formation. (A)** Left,
1080 representative immunoFISH pictures for major satellites and Flag for WT ESCs, grown in
1081 serum, transfected with $TALE_{MajSat}$-Δ or $TALE_{MajSat}$-DAXX. Right, quantification of the number
1082 of major satellite foci detected in the focal plane and corresponding surface area. n=total
1083 number of nuclei for number and foci for sizes analyzed. Two-sided Mann-Whitney tests were
1084 used for statistical analysis. **(B)** Left, mobile fractions of GFP-HP1α calculated from data
1085 presented in Fig. 4D. n=total number of cells analyzed from 2 biological replicates. Right,
1086 fluorescence recovery curves generated for FRAP experiments in WT or *Daxx* KO cells in
1087 serum or ground-state condition. **(C)** MNAse digestion for indicated times in minutes (min.) in
1088 WT or *Daxx* KO cell lines. Total DNA is revealed on a BET agarose gel and Major satellites
1089 via a Southern blot experiment. Right, intensity values of total DNA or major satellite signals,

1090 according to fragment size, from 4min of MNase digestion. One experiment is shown from 2
1091 biological replicates.

1092 **Fig. S6 | Quantification of PML at chromocenters. (A)** Representative field of ESCs grown
1093 in serum or 2iV after immuno-detection of H3K9me3 (red), PML (green) and counterstaining
1094 with DAPI (cyan). Scale bar = 10µm. **(B)** Distribution of PML foci volume observed in WT ESCs
1095 grown in serum (black) or in 2iV (red) from 3 independent replicates. Dashed line indicates the
1096 threshold used to defined large PML foci. **(C)** Boxplots of DAPI signals intensities observed
1097 under small and large PML foci in serum (white) and 2iV (red) conditions. **(D)** Boxplot of
1098 H3K9me3 signals intensities observed under small and large PML foci in serum (white) and
1099 2iV (red) conditions. **(E)** Representative nucleus of ESCs grown in 2iV after immuno-detection
1100 of H3K9me3 (red), PML (green) and counterstaining with DAPI (cyan) presenting a PML-arc
1101 around a PCH cluster (white arrow). Scale bar = 2µm. Two-sided Mann-Whitney tests were
1102 used for statistical analysis in B and D.

1103 **Fig. S7 | Impact of *Pml* deletion on nuclear periphery. (A)** Representative field of WT, *Daxx*
1104 KO and *Pml* KO ESCs, in serum or 2iV after IF against PML (green) and counterstaining with
1105 DAPI (cyan). **(B)** Representative nuclei after immuno-detection of LaminB1 (red) and
1106 counterstaining with DAPI (blue) in WT and *Pml* KO ESCs in serum and 2iV (scale bar = 2µm).
1107 Linescans represent straighten LaminB1 signal at the nuclear periphery (black). **(C)** Boxplots
1108 of LaminB1 signal quantification enrichment at the nuclear periphery from 2 independent
1109 replicates. WT values are taken from Fig. S2D. Two-sided Mann-Whitney tests were used for
1110 statistical analysis.

1111 **Fig. S8 | DAXX recruits SETDB1 to pericentromeres. (A)** Representative
1112 immunofluorescence pictures for SETDB1, DAXX and PML in WT or *Daxx* KO ESCs in serum
1113 condition. **(B)** Top, representative immunofluorescence pictures for SETDB1, DAXX and PML
1114 in WT ESCs in serum. (**C)** Representative immunofluorescence pictures for SETDB1 and Flag-
1115 TALE in *Daxx* KO serum ESCs transfected with $TALE_{MajSat}$ (t_{MS}-Δ), $TALE_{MajSat}$-DAXX (t_{MS}-
1116 DAXX) or $TALE_{MajSat}$-$DAXX^{Y222A}$ (t_{MS}-DAXXY222A). White dashed squares highlight DAPI-

1117 dense Flag-positive chromocenters. **(D)** Quantification of SETDB1 recruitment to Flag-positive
1118 chromocenters. Histogram represents mean with SEM from at least 2 biological replicates.
1119 n=total number of nuclei analyzed. Chi-square tests were used for statistical analysis.

1120 **Fig. S9 | Role of H3.3 and H3K9me3 modifications at PCH. (A)** Representative
1121 immunoFISH pictures for H3K9me3 and DNA FISH of major satellites (MajSat) in both WT and
1122 *Daxx* KO ESCs in serum or ground-state (2iV) conditions. **(B)** Mean and SEM of fluorescence
1123 intensity of H3K9me3 measured over major satellite signal. n=total number of nuclei analyzed
1124 from two independent replicates. **(C)** Quantification of the percentage of cells displaying
1125 H3K9me3 recruitment at Flag-DAPI-dense PCH in Suv39dKO serum ESCs transfected with
1126 $TALE_{MajSat}$-Δ, $TALE_{MajSat}$-SUV39H1, $TALE_{MajSat}$-SETDB1, $TALE_{MajSat}$-DAXX or $TALE_{MajSat}$-
1127 $DAXX^{Y222A}$ grown in serum transfected with $TALE_{MajSat}$-Δ, $TALE_{MajSat}$-DAXX or $TALE_{MajSat}$-
1128 DAXXY222A. T-tests were used for statistical analysis. **(D)** Represents signal after Flag-TALE
1129 immunoprecipitation. Bottom line represents input line from total extract. **(E)** Representative
1130 immunofluorescence pictures of HA-H3.3 in WT cells grown in serum transfected with
1131 $TALE_{MajSat}$-Δ, $TALE_{MajSat}$-DAXX or $TALE_{MajSat}$-$DAXX^{Y222A}$. **(F)** quantification of H3.3 recruitment
1132 at DAPI-dense chromocenters in the indicated Tale-transfected cells. Histogram represent
1133 mean with SEM from at least 2 biological replicates. n=total number of nuclei analyzed. T-tests
1134 were used for statistical analysis. **(G)** Western blot showing the amount of TALE and H3.3
1135 variants in *Daxx* KO ESCs grown in serum transfected with the indicated constructions.

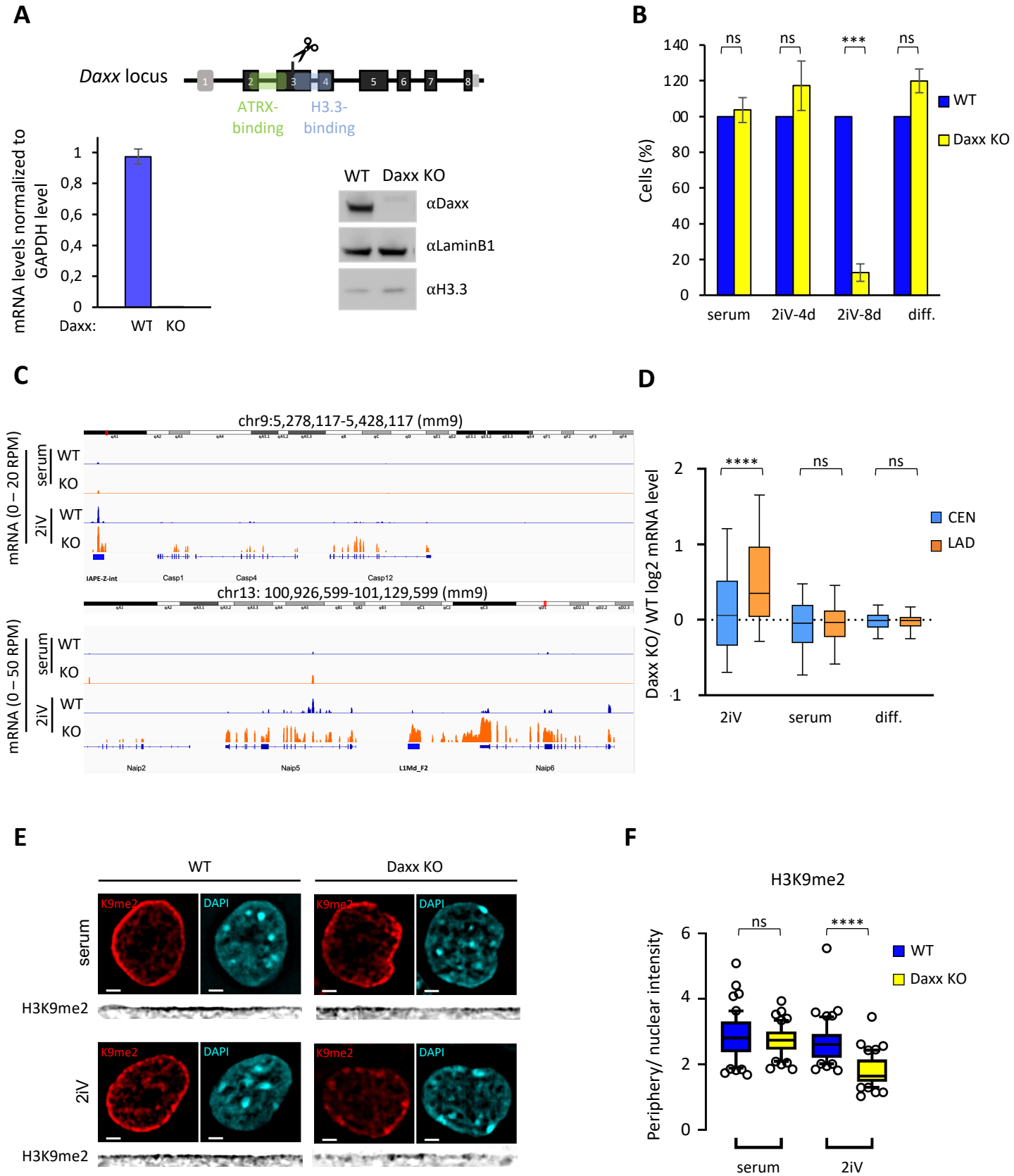

Figure 1. Canat et al. 2023

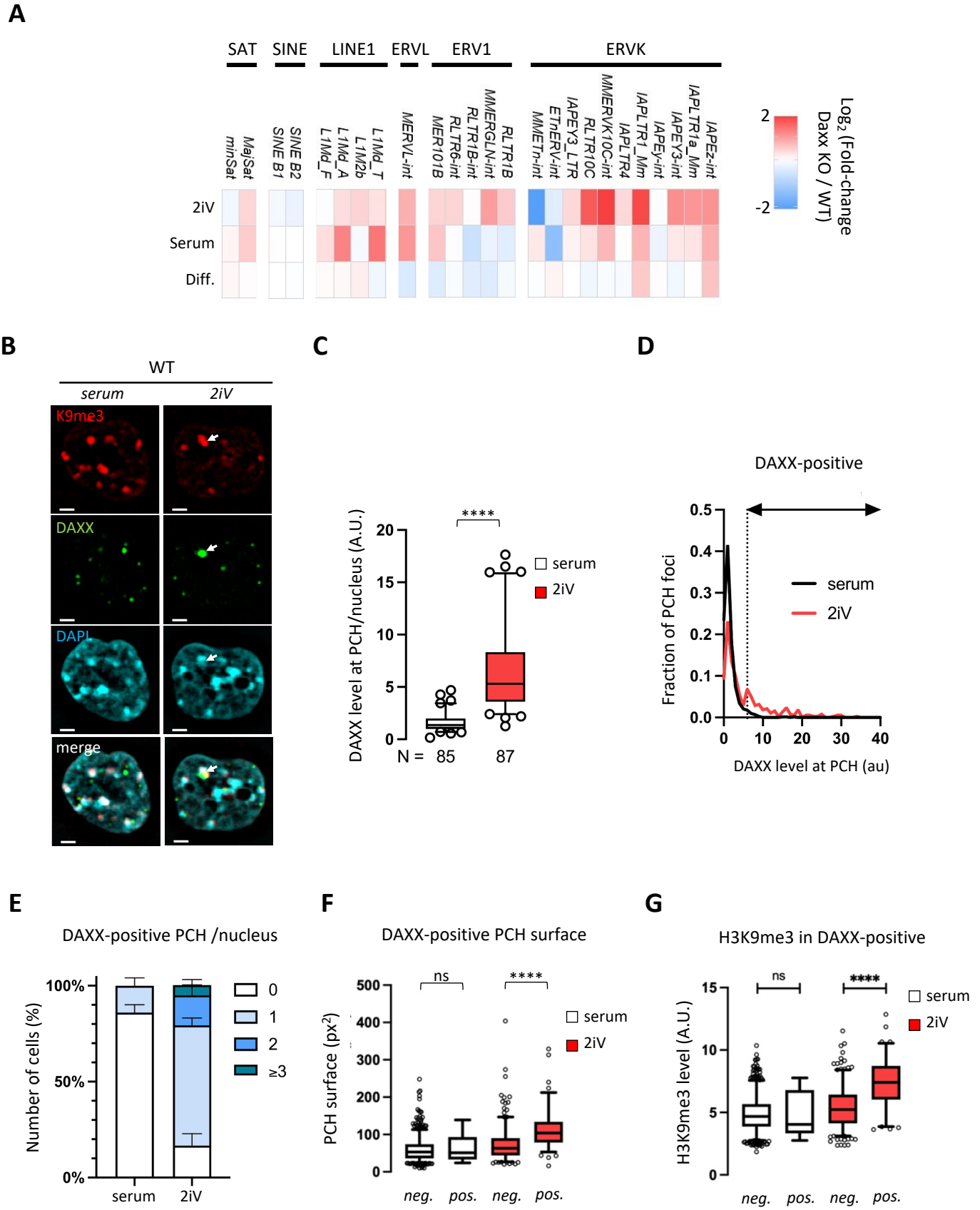

Figure 2. Canat et al. 2023

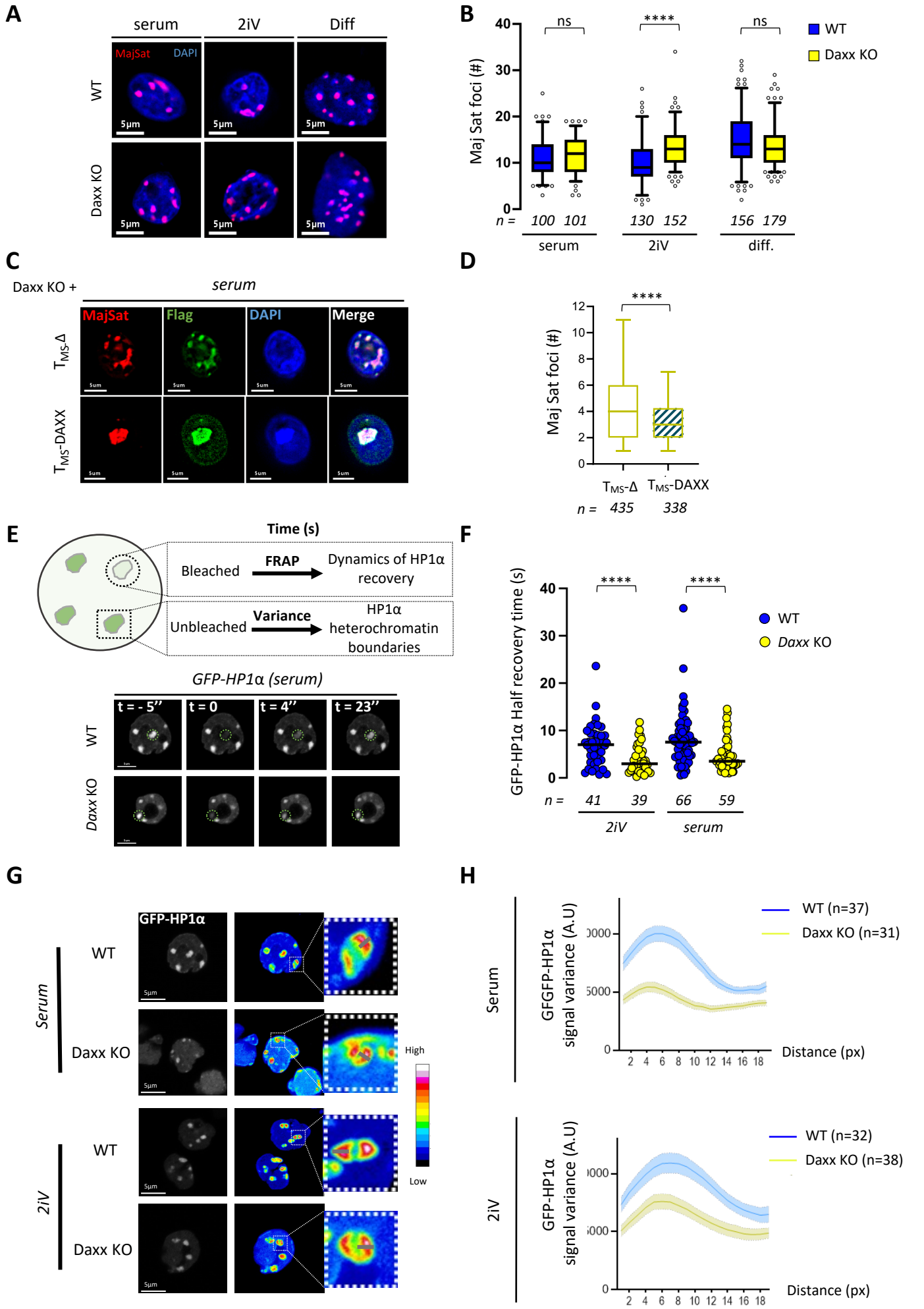

Figure 3. Canat et al. 2023

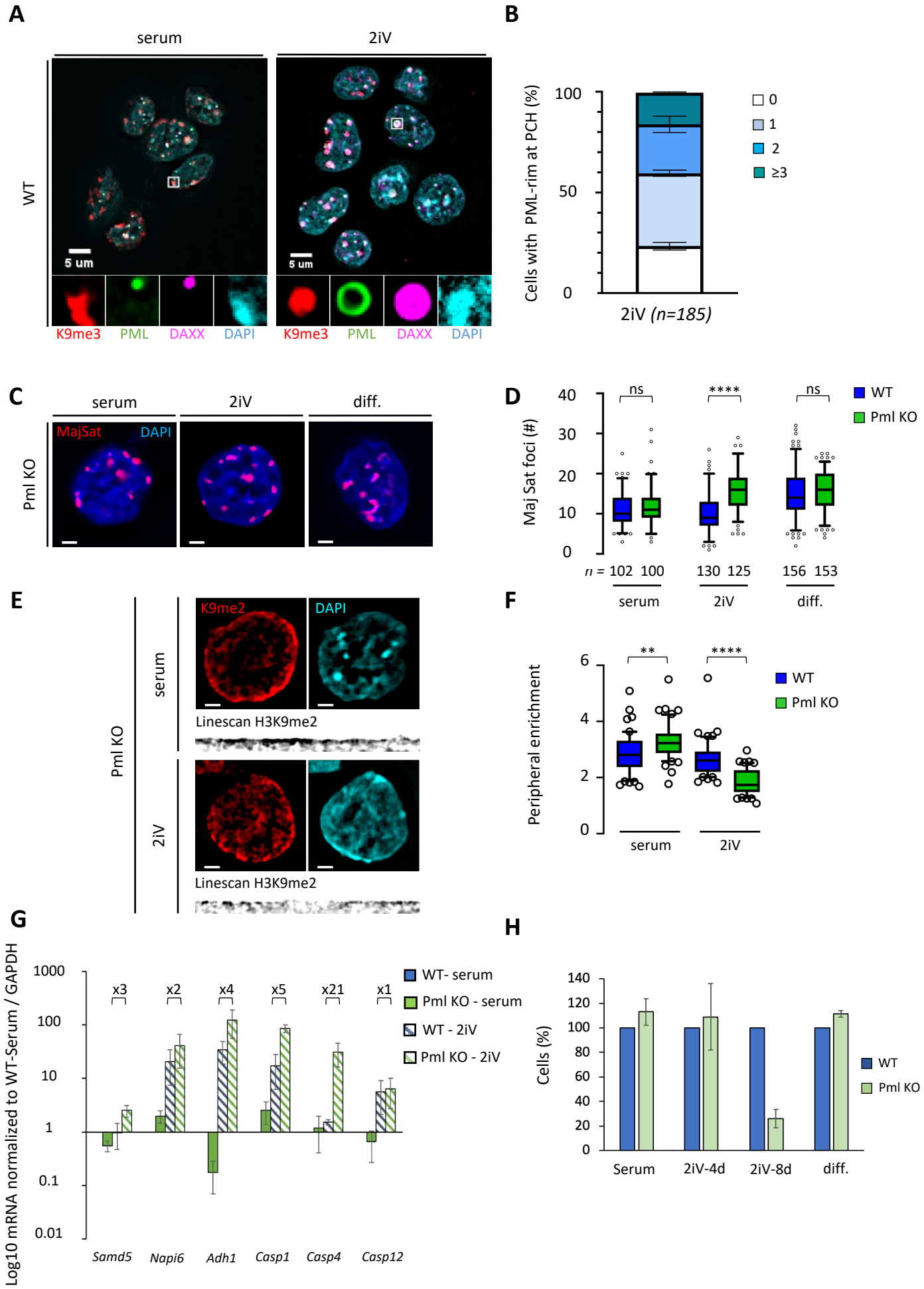

Figure 4. Canat et al. 2023

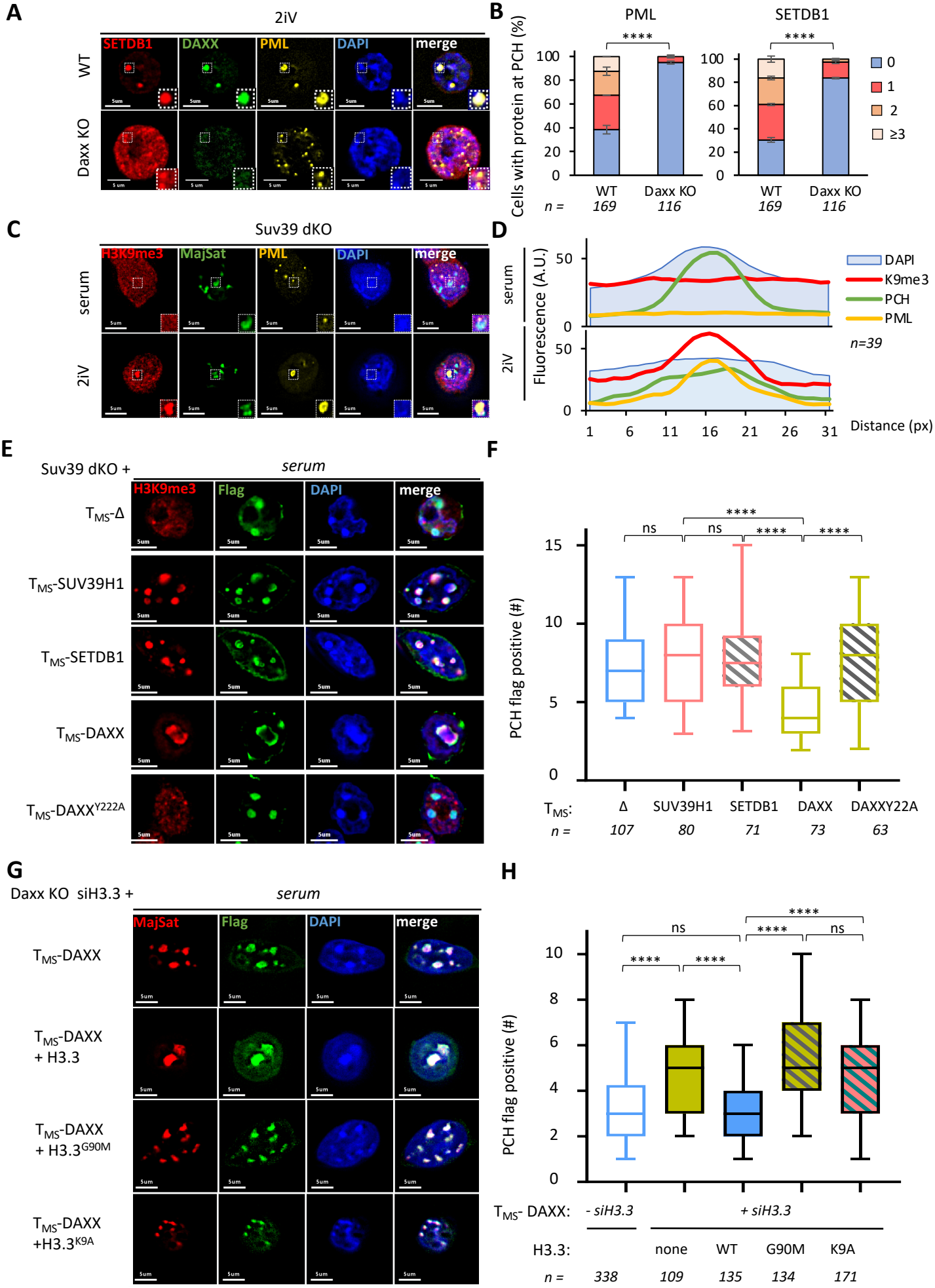

Figure 5. Canat et al. 2023

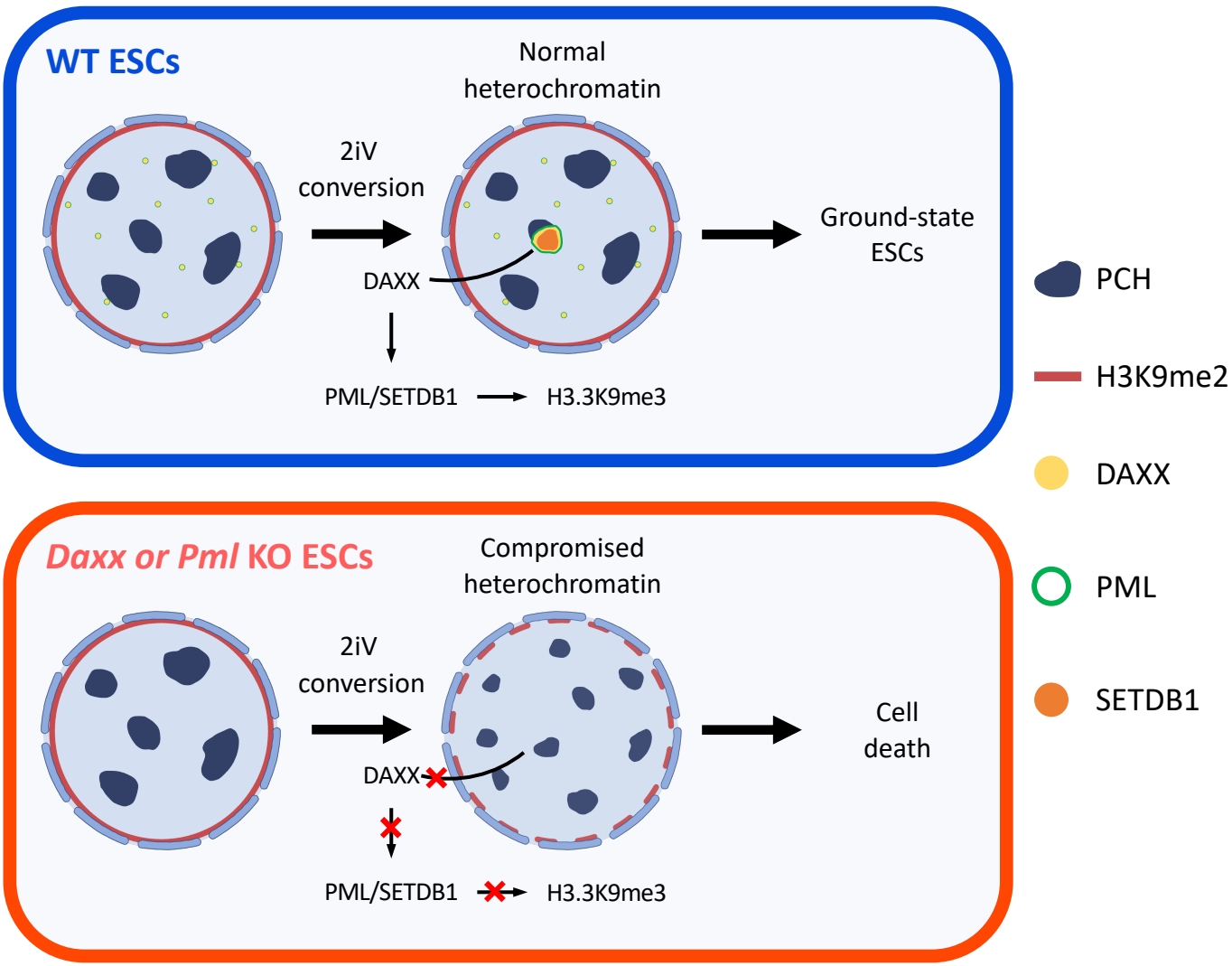

Figure 6. Canat et al. 2023